Setting up a nanolab inside a transmission electron microscope for two-dimensional materials research

Yuting Shen and Litao Sun[a)]
SEU–FEI Nano–Pico Center, Key Lab of MEMS of Ministry of Education, Collaborative Innovation Center for Micro/Nano Fabrication, Device and System, Southeast University, Nanjing 210096, People's Republic of China

(Received 1 June 2015; accepted 16 September 2015)

Two-dimensional (2D) materials, such as graphene, hexagonal boron nitride, and molybdenum sulfide (MoS_2), have attracted considerable interest from the academia and industry because of their extraordinary properties. With the remarkable development of transmission electron microscope (TEM), nanolabs can be established inside the TEM to simulate a real environment by introducing external fields, such as electron irradiation, thermal excitation, electrical field, and mechanical force, into the system. In consequence, besides static structural characterization, in situ TEM can also realize dynamic observation of the evolution in structures and properties of 2D materials. This extension promises an enormous potential for manipulating and engineering 2D materials at the atomic scale with desired structures and properties for future applications. In this study, we review the recent progress of in situ electron microscopy studies of 2D materials, including atomic resolution characterization, in situ growth, nanofabrication, and property characterization.

I. INTRODUCTION

Graphene, as the first 2D atomic crystal,[1] possesses supreme properties, such as extreme mechanical strength, excellent electronic and thermal conductivities, high surface area, and impermeability to gas.[2] Given these properties, graphene is feasible for applications in various fields, including electronics, photonics, composite materials, paints and coatings, energy generation and storage, sensors and metrology, and bioapplications.[3] However, graphene is unlikely to be used for fabricating high-performance integrated logic circuits because of the absence of a band gap. Scientists have explored alternative materials, including structurally related 2D materials, such as hexagonal boron nitride (h-BN),[4] transition metal dichalcogenides,[5] layered transition oxides, and topological insulators of bismuth telluride (Bi_2Te_3) and bismuth selenide (Bi_2Se_3), which have gained extensive interest.[6] Like graphene, these 2D materials are important in various applications because of their distinct properties. Since the novel 2D materials will function significantly in the future development of materials, discovering the essential relationship between their structure and properties is vital.

Transmission electron microscope (TEM) has undergone remarkable development, and achieved atomic resolution by the inclusion of aberration correctors and other techniques, such as monochromators, in recent years.[7–9] TEM has become an indispensable tool for detailed characterization of the atomic structures of 2D materials. With a full understanding of atomic structures of 2D materials, further investigating the structural evolution and structure–property relationships in a real environment is feasible. We can simulate a real environment by introducing external fields, such as electron irradiation, thermal excitation, electrical fields, and mechanical force, into a TEM. These modifications are called in situ TEM experiments. Electron irradiation can be easily realized or expected in TEM. Detailed in situ experiments have been carried out to study electron irradiation induced structural evolution[10–15] and nanofabrication[16,17] of 2D materials. Other in situ TEM characterizations can be realized by specialized holders, including scanning tunneling microscope (STM) holders, electrical bias, heating, cooling, mechanical, and liquid cell holders.[18]

Moreover, with the development of ultrafast imaging,[19–24] real-time monitoring of dynamic processes, such as chemical reaction, structure reconstruction, defect generation and migration, and property evolution under various external fields, is feasible. In consequence, TEM served as a nanolab for 2D materials. In this article, we review atomic resolution characterization, in situ growth, nanofabrication, and property characterization of 2D materials, such as graphene, h-BN, and transition metal dichalcogenides (TMDs).

II. ATOMIC RESOLUTION CHARACTERIZATION

With the rapid development of modern TEM technology, TEM has become an indispensable tool for characterizing interior[12,25–30] and edge structure,[10,29,31,32] defects,[14,32–39]

Contributing Editor: Eric A. Stach
[a)]Address all correspondence to this author.
e-mail: slt@seu.edu.cn
This paper has been selected as an Invited Feature Paper.
DOI: 10.1557/jmr.2015.304

 © Materials Research Society 2015

https://doi.org/10.1557/jmr.2015.304 Published online by Cambridge University Press

grain boundaries[26,40–42] and stacking[12,43,44] of 2D materials at atomic resolution. However, electron irradiation is inevitable and adversely affect the specimen through heating, electrostatic charging, radiolysis, displacement damage, sputtering, and hydrocarbon contamination.[45] Considering that structural alterations of materials have occasionally been misinterpreted as a structural property, the use of low-voltage TEM equipped with modern aberration correctors for observing 2D materials is important to minimize radiation damage.[6,46] Understanding the atomic structures of 2D materials is of considerable significance for further investigation under different external stimuli.

A. Graphene

As the most investigated representative of the 2D materials, the irradiation effects of graphene have been studied first. Knock-on atom displacements are known as the main source of radiation damage in graphene. Electron beams with an acceleration voltage of 80 kV do not damage graphene, because the maximum energy transferred to a carbon atom is below the theoretical displacement energy. However, this low voltage does not completely eradicate the sputtering of the under-coordinated carbon atom. Recent work has shown that the formation of vacancy defects depends not only on electron energy but also on beam current density.[47] Normally, we still use the TEM at 80 kV to investigate the production,[14,24,48] migration,[49] reconstruction, and annihilation[14,24] of defects. Without the special version, the acceleration voltage of TEM in this review is 80 kV.

Given that the unique electronic, thermal, and mechanical properties of graphene are sensitive to lattice structure,[40,50] the study of defects in graphene is significantly important. Defects in graphene, such as Stone–Wales (SW) defect, monovacancy (MV), divacancy (DV), tetravacancy, multi-vacancies, adatoms, substitutions, interstitials, and grain boundaries, have been explored under electron irradiation.

1. Stone–Wales defect

A SW defect is formed by an in-plane 90° rotation of a C–C bond, yielding a transformation of four adjacent hexagons to two pentagons and two heptagons.[48] The defect is unlikely to remain stable in TEM, because the relaxation energy required for the defect to revert back to pristine lattice is about 5 eV,[51] which is less than the calculated displacement threshold energy.[51,52] As shown in Figs. 1(a)–1(d), an isolated SW defect was found during one exposure of the sequence and relaxed to an unperturbed lattice 4 s later.[14]

2. Vacancies

The ejection of a carbon atom yields a single vacancy and leaves three dangling bonds in graphene[48] [Fig. 1(i)]. The MV undergoes a Jahn–Teller distortion[54] to minimize the energy of the graphene, forming a band between the two atoms near the vacancy and results in a pentagon and a nonagon [Fig. 1(j)]. The images in Figs. 1(f)–1(h) show a single vacancy absorbing a carbon atom and returning to an unperturbed lattice after several seconds.[14] A DV is formed by sputtering the carbon atom bonded to only two neighbors in MV, thereby leaving no dangling bonds in the graphene.[48] This form is more stable under irradiation, because all of the atoms are sp^2 bonded. Several configurations of DV exist and oscillate among each other,[24,55] as illustrated in Figs. 1(k)–1(m). With ejection of other two atoms, the tetravacancy was generated under electron irradiation. Robertson et al.[53] examined various structural permutations of tetravacancy defects in monolayer graphene by using aberration-corrected TEM and found that two most prevalent structures are extended line defect structures in Figs. 1(q) and 1(r). Not only the formation energy, but also the specific procedure of tetravacancy formation affects the structures of tetravacancy.[53] The formation of multi-vacancies in graphene can be explained by vacancies migrating and agglomerating with electron beam-induced bond rotation and atom removal.[34] Continuous sputtering of atoms in a small area will create a hole in graphene with unsaturated bonds around its circumference. The fabrication and healing of holes in graphene and their potential applications will be discussed in the following nanofabrication section.

3. Adatoms, substitutions, and interstitials

There are three main manners for the dopant atoms to incorporate into graphene lattices and tune their properties: adatoms, substitutions, and interstitials.

Adatoms are typically absorbed to the graphene lattice by van der Waals bonding in the bridge (B), hollow (H), and top (T) sites.[48,56] The foreign atom substituting a carbon atom in the graphene lattice, forming bonds with the surrounding carbon atoms, is substitution.

Vacancies can act as occupancy sites for interstitial impurities to form single-atom dopants that are covalently bonded in the lattice. For instance, a DV in graphene is occupied by a surface iron (Fe) contaminant,[57] forming an interstitial defect, and trivacancy occupied by a platinum (Pt) interstitial.[58]

The doped graphene and migration of dopant under electron irradiation will be elaborated later.

4. Grain boundaries

Chemical vapor deposition (CVD) is an excellent and widely used technique for growing large-area graphene. However, this method may introduce grain boundaries, which influence the characteristics of graphene. Thus, investigating grain boundaries, understanding their structure and structure–property relationship, and ultimately

https://doi.org/10.1557/jmr.2015.304 Published online by Cambridge University Press

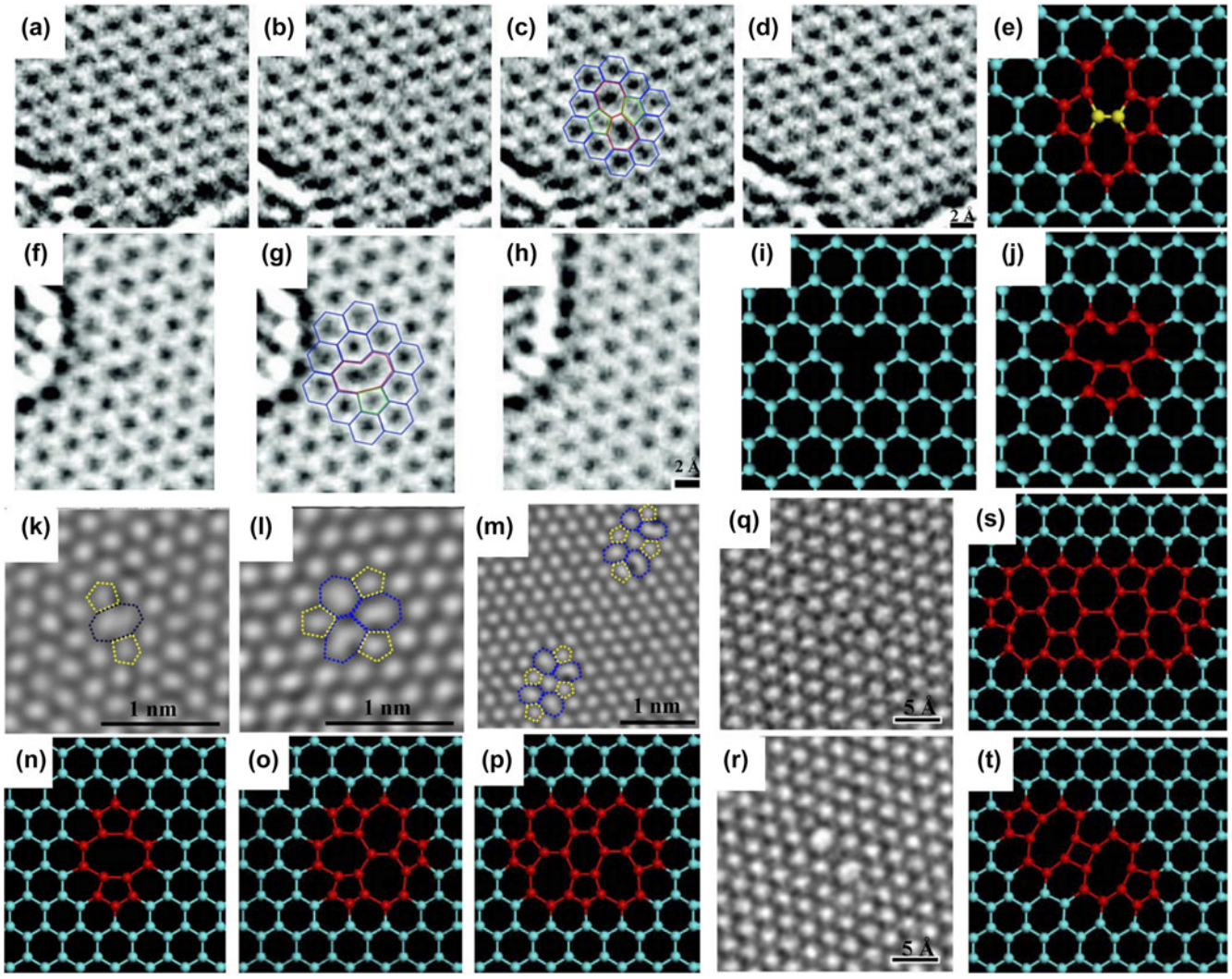


FIG. 1. Different defects in graphene. (a–d) SW defect: (a) unperturbed lattice before the appearance of the defect, (b) SW defect, (c) same image with superimposed atomic configuration, and (d) relaxation to unperturbed lattice (after approximately 4 s). (e) Atomic models of SW defect. Yellow bond indicates the reconstructed bond. (f–h) Reconstructed MV: (f) original image and (g) with atomic configuration, and (h) unperturbed lattice, 4 s later. (i–j) Atomic models of the formation of a reconstructed MV: removal of the carbon atom (i) leads to a metastable configuration that can undergo a Jahn–Teller distortion, reconstructing to form the model in (j). Reprinted with permission from Ref. 14, Copyright 2008, American Chemical Society. (k–m) TEM images of three different types of DVs: (k) (5–8–5) DV, (l) (555–777) DV, and (m) (5555–6–7777) DV. (n–p) Atomic models corresponding to (k–m), respectively. Reprinted with permission from Ref. 24, Copyright 2012, Macmillan Publishers Limited. (q–r) Two most frequently observed tetravacancy defects and (s–t) their corresponding atomic models. Reprinted with permission from Ref. 53, Copyright 2014, American Chemical Society.

engineering grain boundaries to achieve desired properties for future applications are important. Given that various theoretical investigations[40,59–62] on grain boundaries have been conducted, experimentally studying grain boundaries is currently feasible with TEM modern techniques, including scanning TEM (STEM), and high-resolution TEM (HRTEM). The atomic arrangements of grain boundaries can be imaged through STEM and HRTEM.

Grain orientations can be mapped by dark field TEM (DF–TEM), in which individual crystal orientations (gained by selected-area electron diffraction patterns) are isolated by using an aperture to select the appropriate diffraction spot, as shown in Figs. 2(a) and 2(b).[41,63–66] In Fig. 2(c), STEM (operating at 60 kV) image shows the grain boundary between two graphene grains, which have an angle of 27° at atomic resolution. The grain boundary is composed of different defects, like pentagons, heptagons, and distorted hexagons, which are irregularly arranged.[41] The high concentration of defects at the grain boundaries make the grain boundary more chemically reactive than pristine graphene,[60] and offer sites for adsorbates to bind.[41,63]

The grain boundaries mentioned above are arranged by direct atomic bonding, while a distinct configuration existed in a few-layer graphene is overlapping, which

https://doi.org/10.1557/jmr.2015.304 Published online by Cambridge University Press

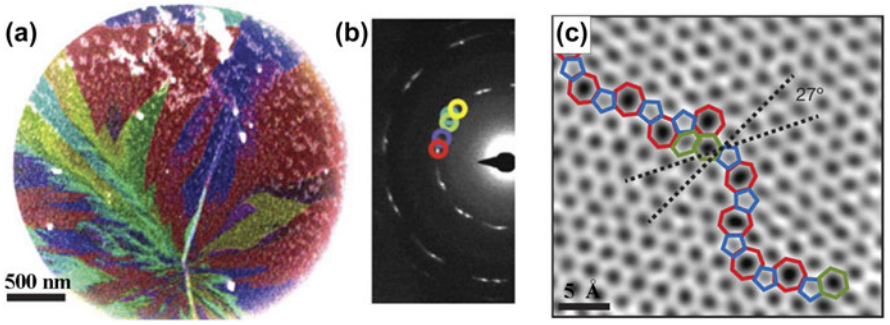


FIG. 2. (a) False color dark-field TEM image of multiple graphene grain orientations. (b) Diffraction pattern of polycrystalline graphene in (a), with the colored circles corresponding to the selected aperture used to highlight the same colored grain in (a). (c) Two grains (bottom left, top right) intersect with a 27° relative rotation. Reprinted with permission from Ref. 41, Copyright 2011, Macmillan Publishers Limited.

one graphene domain grows on the top of a neighboring domain.[65] The two different types of grain boundaries can be distinguished by analyzing the change of diffraction through the grain boundary and the effect of defocus on the contrast of the interface. Overlapping graphene sheets exist an area of superposition of crystal orientations across the grain boundary,[64] and have strong edge contrast with the change of defocus values.[65]

5. Edge structure

Three main configurations of edges in graphene exist, namely, zigzag, armchair, and reconstructed (pentagon–heptagon) zigzag and klein edges.[48,67] Investigating the dynamics of graphene edges is of considerable significance as edge structures, properties, and their functionalization crucially influence the conductive, mechanical, elastic, and chemical properties of graphene nanoribbons.

In theory, graphene sheets with zigzag edges are not stable compared with that of the graphene sheets with armchair edges.[68,69] Experimentally, Kim et al.[70] fabricated clean and atomically smooth graphene edges in zigzag, armchair, and reconstructed zigzag configurations by electron beam-induced mechanical tearing. They found that the zigzag edge can be completely and reversibly transform between the hexagon–hexagon zigzag edge and pentagon–heptagon reconstructed zigzag edge under electron irradiation, while the armchair edge is relatively stable, with short zigzag edge segments embedded.

Notably, Girit et al.[10] and Warner et al.[71] demonstrated that the zigzag edge of the hole is more stable than the armchair edge under electron irradiation at 80 kV.[10] Koskinen et al.[11] analyzed the data from the successful experiment taken by Girit et al.[10] and demonstrated the existence and stability of the reconstructed zigzag edge, which is the most stable graphene edge. These results vary considerably from other theoretical and experimental findings of an open edge mentioned above. The reason is that, there are under-coordinated carbon atoms at the rim of the graphene hole with an equal probability to be sputtered, which results in the zigzag edges.[68]

Graphene edges functionalized by hydrogen are the most elusive to study because of the small atomic mass of hydrogen. In theory, unlike hydrogen attachment, hydrogen-free armchair edges undergoes strong reconstruction and leads to a reduction of the bond lengths, which is likely to form a triple bond.[72] Therefore, He et al.[73] first indirectly determined whether graphene edges are hydrogenated by measuring the C–C bond lengths in armchair graphene edges and demonstrated that the graphene edges are not always hydrogenated. Furthermore, the group tracked the bond lengths in real time, and found that the lengths increased when the armchair edge being functionalized by an additional atom and form a triangle–hexagon structure while decreased to the same C–C bond upon the removal of the additional atom.

However, there are various defects and chemical functionalization upon the graphene edges, which make the edge structure not perfect.[70] Heat treatment can reduce the amount of defects near all edges of graphene, and most of the thermally treated graphene edges are completely closed due to the reduced number of dangling carbon bonds.[74] For open edges under high-temperature annealing, most of the configurations are armchair-type, whereas the zigzag-type comprise the least configurations.[75]

Studies about atomic structures of graphene have important significance for understanding and optimizing the properties of graphene, which provide a building block for realizing the ultimate promise of fabricating various devices for future applications.

B. Other 2D materials

Since the discovery of the extraordinary properties of graphene, a diverse source of 2D layered materials, such as h-BN, MoS_2, $MoSe_2$, tungsten disulfide (WS_2), and other 2D compounds, has boosted great interest. These materials offer unique properties that differ from those of

https://doi.org/10.1557/jmr.2015.304 Published online by Cambridge University Press

graphene and would be useful in applications ranging from electronics to energy storage.

1. Boron nitride (BN)

h-BN presents the closest structural similarity to graphene, consisting of equal numbers of boron and nitrogen atoms in a honeycomb arrangement. However, the slightly ionic bonding in- and out-of-plane, and its electrically insulating characteristic with a large band gap distinguish h-BN from graphene.[76] Furthermore, unlike the ABA stacking of graphite, h-BN layers are stacked by AAA structure, which the boron and nitrogen atoms stack directly on top of each other.[29] Ultrahigh resolution TEM has been applied to identify the structures, defects, and grain boundaries of h-BN. Single-layer h-BN can be fabricated by employing high-energy electron beam to sputter off subsequent layers one-by-one from BN membranes.[30,37]

Directly identifying the boron and nitrogen atoms is necessary so that the lattice defects, edge structure, and grain boundaries in h-BN can be clarified. In recent works, individual boron and nitrogen atoms can be discriminated by the intensity profile of TEM reconstructed phase images[29,30] and STEM annular dark field (STEM–ADF) images[77] [Figs. 3(a)–3(d)]. In these representations, nitrogen yields stronger intensity than boron.

The threshold energy for the knock-on damage of boron and nitrogen atoms is 74 and 84 keV,[78] respectively, thereby sputtering boron atoms to form MVs in TEM with an acceleration voltage of 80 kV is more advantageous.[29] At 120 kV, the energy carried by incident electrons is larger than the threshold energy of both atoms, and boron atoms remain more prominent for ejection.[30] A mild local reconstruction occurs around the missing boron atom, where distances between pairs of nitrogen atoms surrounding the MV are slightly larger than those in a perfect h-BN.[30] Besides boron MVs, a large amount of triangle-shaped vacancies with different sizes exist in h-BN [Fig. 3(e)].[37] The image in Fig. 3(f) schematically shows the smallest triangle vacancy with three missing boron atoms and one nitrogen atom.[29] Remarkably, all triangle-shaped defects in single-layer h-BN are in the same orientation, which indicates that all atoms that are knocked out by the electron beam must be of the same type and that boron and nitrogen vacancies cannot coexist.[30,37] In addition, SW defects and topological defects, such as pentagon or heptagon, which are commonly found in graphene, have not been discovered in h-BN.[29,30,37] Any bond rotation or local reconstruction around missing boron atoms, which may form B–B or N–N bond, requires large activation energy.[30] However, in recent research, at an elevated temperature, Cretu et al.[36] observed tetragon–octagon defects with B–B and N–N bonds, which is contradictory from the results mentioned above. The defects migrated via atomic row gliding along the armchair direction under electron irradiation.[36]

Edge structure plays a crucial role in the properties of h-BN; thus, determining the edge structure of h-BN is important. Different edge configurations have been examined through defects, holes, and atomic step edges. Two prominent edge configurations exist, namely, nitrogen-terminated zigzag edges and boron–nitrogen armchair edges [Figs. 3(g) and 3(h)].[29] Nitrogen-terminated zigzag edges are elucidated to be more stable under electron irradiation because of the lower knock-on energy threshold of boron and the tendency for zigzag structures in planar sp^2 bonded 2D materials.[29,30] Gibb et al.[35] reported the first HRTEM observation of grain boundaries in h-BN via in situ heating. The group found several pentagon and heptagon defects along the grain boundary, which are unexpected in h-BN sheets [Fig. 3(j)].

In few-layer h-BN, Warner et al.[12] observed the dynamic process of nanopatterning under continuous electron irradiation with accelerating voltage of 80 kV. They found that the defects evolve into triangular nanopatterns in most cases, and occasionally hexagonal patterns as well. The preferential edge structure of nanopatterns is zigzag, and the zigzag edges may reconstruct to armchair edges during sputtering process.

Given the nearly identical lattice constant of h-BN with graphene, composite devices can be fabricated. For example, the use of h-BN as a template for graphene can open the band gap in graphene.[79]

2. MoS_2

In addition to graphene and h-BN, single-layer MoS_2 is a newly emerging 2D material with potential applications in electronics, optoelectronics, and energy storage.[25,80,81] MoS_2 is a semiconductor with band gap of 1.1–2 eV.[81,82]

As shown in Fig. 4(a), two atomic layers of closed-packed sulfur atoms are separated by one close-packed Mo atomic layer in a single layer MoS_2, which imparts its defects structures with more complexity than those in graphene or h-BN. In theory, the displacement energy for sulfur atoms in the bottom layer is approximately 6.9 eV, which indicates that the corresponding threshold energy is 90 kV.[32] Therefore, 80 keV electron beam imaging cannot generate single-sulfur vacancy in MoS_2. For sulfur atoms at the top layer, the displacement energy even exceeds 8.1 eV,[32] which results in prominent formation of single-sulfur vacancies in comparison with double-sulfur vacancies. However, continuous 80 keV electron irradiation can eventually induce the sputtering of sulfur atoms and create sulfur vacancies in MoS_2.[32] Sulfur vacancy can be distinguished by analyzing the intensity profile.[39] Figure 4(b) shows the comparison between intensity profiles along the lattice with (red symbol) and without (black symbol) single-sulfur vacancy, which quantitatively correspond to the simulated HRTEM image (red solid line).[39] Under continuous electron

https://doi.org/10.1557/jmr.2015.304 Published online by Cambridge University Press

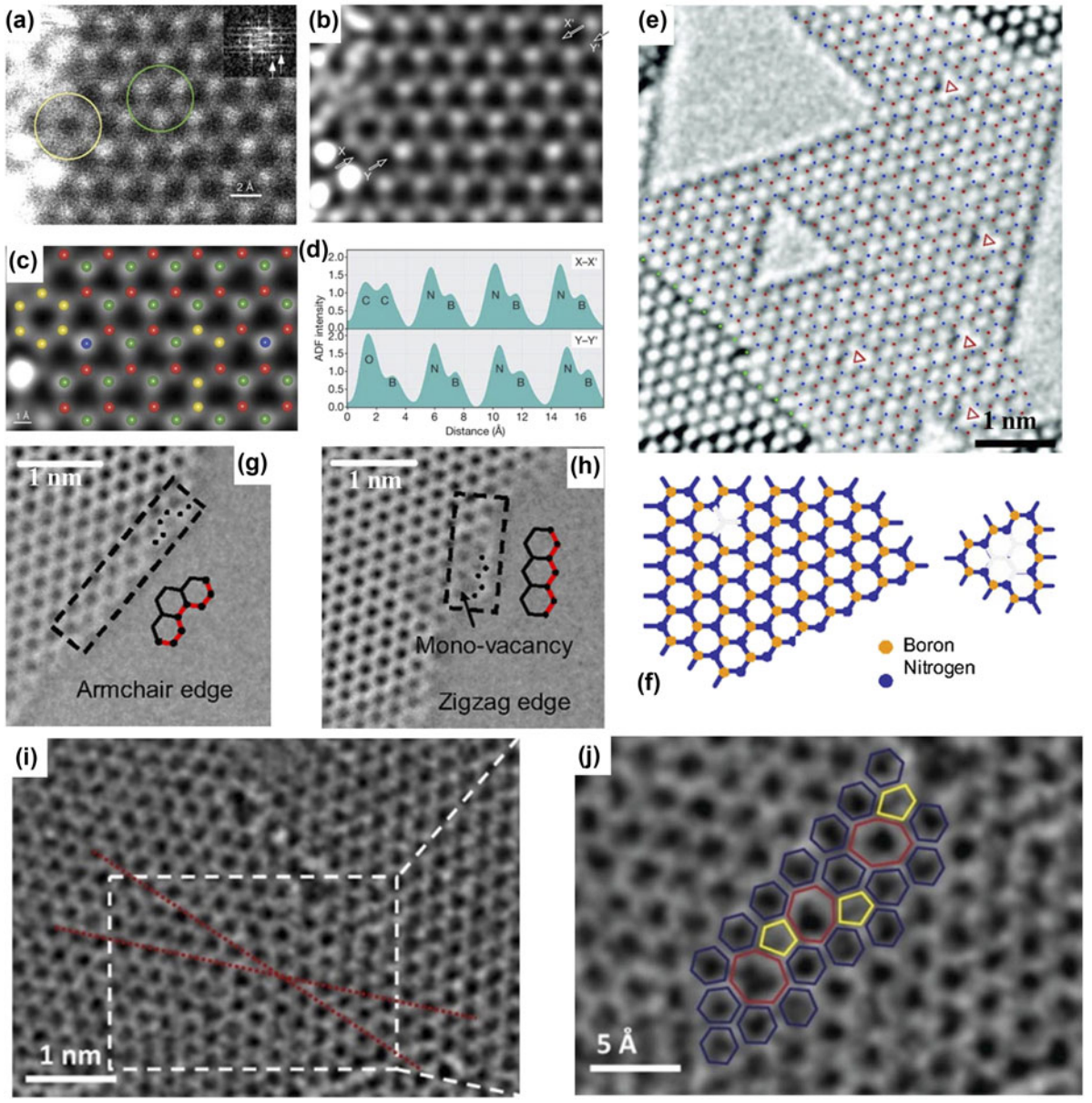


FIG. 3. (a) Original and (b) smoothed STEM–ADF images of monolayer BN and (c) with an overlaid structural model: Red, Boron; yellow, Carbon; green, Nitrogen; blue, Oxygen. (d) Line profiles of the image intensity along X–X' and Y–Y' in image (b). Reprinted with permission from Ref. 77, Copyright 2010, Macmillan Publishers Limited. (e) Single-layer h-BN membrane with different sizes of triangle-shaped vacancies. Red triangles indicate the boron monovacancies. Reprinted with permission from Ref. 37, Copyright 2009, American Chemical Society. (f) Schematic morphology of the boron MV and the smallest triangle-shaped vacancy. (g–h) HRTEM images of BN edge structures: (g) Zigzag edge and (h) armchair edge. Reprinted with permission from Ref. 29, Copyright 2009, American Physical Society. (i) Grain boundary in a monolayer of h-BN with a misorientation angle of 21°. (j) Magnified grain boundary defect structure from the inset of (i), hexagon, heptagon, and pentagon structures are depicted in blue, red, and yellow, respectively. Reprinted with permission from Ref. 35, Copyright 2013, American Chemical Society.

irradiation, the sulfur vacancies tend to migrate and agglomerate to form line defects.[38]

Zhou et al.[83] systematically investigated the defects in CVD grown monolayer MoS_2 by utilizing ADF imaging on aberration-corrected STEM. The image intensity of STEM–ADF is directly related to the atomic number, which allows unambiguous atom-by-atom chemical identification. The research group observed six different configurations of defects in MoS_2, namely, single-sulfur vacancy, double-sulfur vacancy, Mo vacancy complex of Mo and nearby three sulfur atoms, vacancy complex of Mo and nearby three disulfur pairs, anti-site defects where a Mo atom substitutes for a disulfur column, and those where a disulfur column substitutes for a Mo atom, as shown in Figs. 4(c)–4(h).[83] Due to the lowest formation energy of all defects, single-sulfur vacancies

https://doi.org/10.1557/jmr.2015.304 Published online by Cambridge University Press

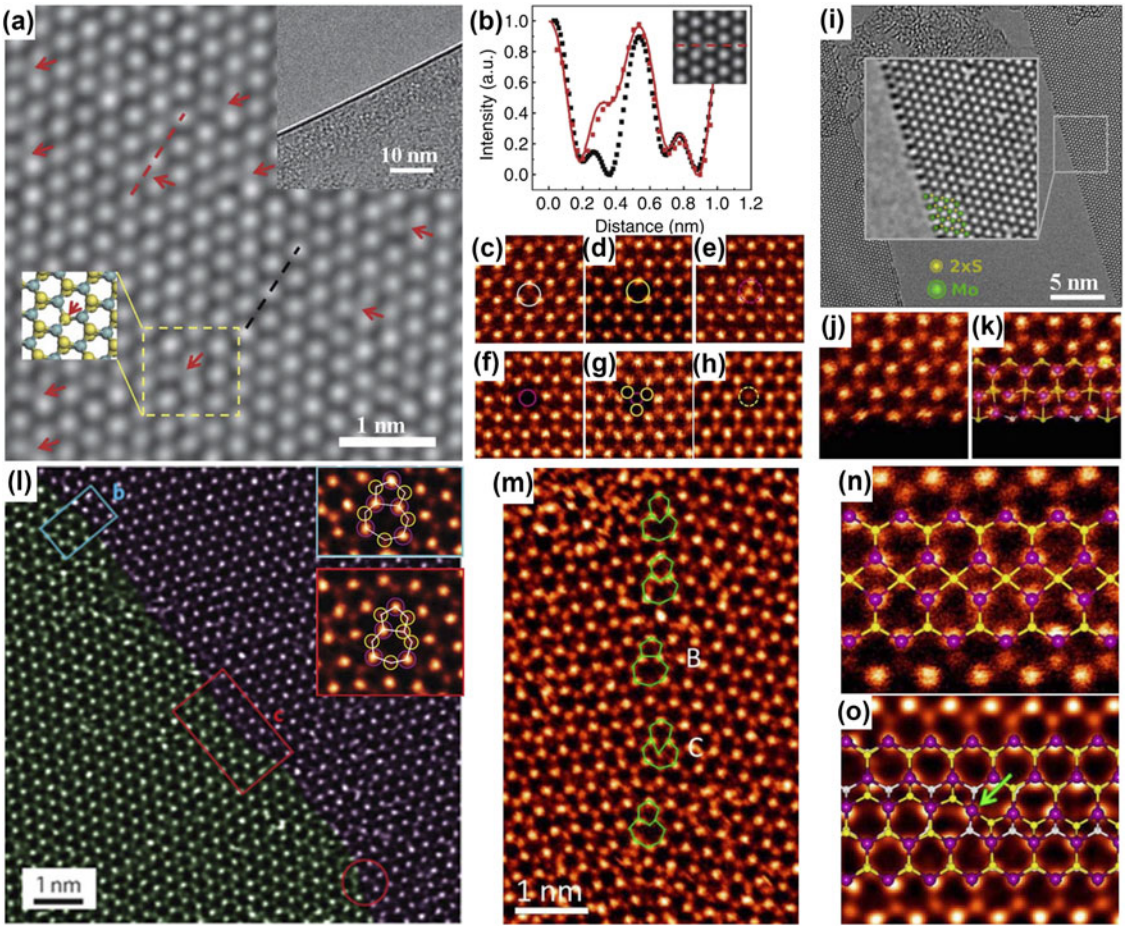


FIG. 4. (a) AC–TEM image of the atomic structures of a single-layer MoS_2. Red arrows indicate sulfur vacancies. Upper inset shows the edge of a single-layer MoS_2. Lower inset shows the schematics of the highlighted region. Blue and yellow dots represent Mo and S atoms, respectively. (b) Intensity profile along lattices with (red symbol) and without (black symbol) sulfur vacancy, along with simulations of a single-sulfur vacancy (red line). The corresponding sections are highlighted in (a) by dashed lines. Inset shows the simulated TEM image of a single sulfur vacancy. (c–h) STEM–ADF images of six different defect configurations in MoS_2. (i) AC–TEM images of MoS_2 edge structure terminated with Mo atom. (j) STEM–ADF image of regular Mo-terminated edge. (k) STEM–ADF image of reconstruction of the Mo-terminated edge with the overlaid structural model. (l) STEM–ADF image of a MoS_2 grain boundary. Insets are the zoom-in views of common dislocations highlighted by the blue and red rectangles. Purple and yellow circles are Mo and S_2 columns, respectively. (m) STEM–ADF images of an 18.5° grain boundary consisting of dislocations with pentagon and heptagon and dislocations with hexagon and octagon. (n) STEM–ADF image of the 4|4P 60°-grain boundary structure with the overlaid structural model. (o) STEM–ADF image and overlaid structural model of a 4|4E 60°-grain boundary. The grain boundary steps are linked by 4-fold coordinated Mo atoms as highlighted. (a and b) Reprinted with permission from Ref. 39, Copyright 2013, Macmillan Publishers Limited. (c–h, j–k, and m–o) Reprinted with permission from Ref. 83, Copyright 2013, American Chemical Society. (i) Reprinted with permission from Ref. 32, Copyright 2012 American Physical Society. (l) Reprinted with permission from Ref. 26, Copyright 2013, Macmillan Publishers Limited.

were found considerably more frequently than double-sulfur vacancies, which is quite different from graphene for DVs are energetically more stable.[83,84]

Under continuous electron irradiation, a crack is formed in the MoS_2 membrane with the edge of Mo-terminated, as illustrated in Figs. 4(i).[32] In addition to the regular Mo-terminated edge [Fig. 4(j)], a new type of edge reconstruction [Fig. 4(k)] is discovered, in which the outmost row of Mo atoms move closer to the inner Mo row, and the sulfur atoms at this reconstructed edge are monosulfur rather than disulfur.[83]

Similar to grain boundaries in graphene, pentagon–heptagon dislocation cores are found in MoS_2. As shown in Fig. 4(l), the pentagon and heptagon rings are Mo-oriented (blue rectangle labeled) or with sulfur substituted one of the Mo sites (red rectangle labeled).[26] The common pentagon–heptagon dislocations along the grain boundaries were also observed by Zhou et al.,[83] which easily transferred to hexagon–octagon dislocations by incorporating monosulfur or disulfur into Mo–Mo bonds under sulfur-rich conditions [Fig. 4(m)]. Furthermore, the group explored several exceptional grain boundaries in MoS_2 that were distinctly different from those in graphene. Figure 4(n) shows 4|4P type grain boundary, where the sulfur atoms at the grain boundary are bonded to four Mo atoms rather than three, whereas Mo atoms

https://doi.org/10.1557/jmr.2015.304 Published online by Cambridge University Press

retain the regular 6-fold coordination. Another 4|4E type grain boundary is illustrated in Fig. 4(o); the two grains shifted laterally by half of a lattice constant along the grain boundary. The Mo atoms at the grain boundary are linked with four sulfur sites and the disulfur sites are substituted with monosulfur atom.

The in-depth atomic scale studies of structure and defects in MoS_2 offer new opportunities for understanding structure–property relationship and future controlling the grain growth of MoS_2.

Other 2D TMDs such as WS_2[27] and $MoSe_2$[13] have emerged and generated substantial interest because of their specific properties. However, the in situ investigation of their structures, defects and properties is at the beginning stage, and considerable work still needs to be carried out.

III. IN SITU GROWTH OF 2D MATERIALS

Various techniques can be used to produce suitable graphene and other 2D materials layers, such as mechanical exfoliation, liquid-phase exfoliation, CVD, and molecular beam epitaxy. All these methods have their own advantages and disadvantages. A profound insight into the mechanism of nucleation and growth of 2D materials in real time by TEM is important so that we can precisely control the growth process and produce the desired materials. In situ growth of carbon nanotubes has already been investigated for decades. However, few experiments[75,85–91] have been conducted to study the growth mechanism of 2D materials because of the difficulty in introducing source materials into high-vacuum TEM.

A. In situ growth of graphene

For most studies, graphene is grown by metal-catalyzed solid-state transformation of carbon at elevated temperatures. Rodriguez–Manzo et al.[85] deposited thin polycrystalline layers of Fe, Co, and Ni onto amorphous carbon film and increased the temperature to above 600 °C. The metal crystals began to migrate to grow thin metal layers under electron irradiation or to coalesce to form metal islands at high temperatures over the amorphous carbon films. Subsequently, the amorphous carbon films under the metal layers were dissolved, and graphene sheets began to nuclear and grow. At sufficiently high temperature, they observed the graphene by tracing the retraction of metal crystal, as shown in Figs. 5(a)–5(c). The same phenomenon was reported by He et al.[86] whose observations showed graphene sheets formed by utilizing Joule heating under a large bias voltage to extract Ag nanowire covered with thin amorphous carbon sheath. Westenfelder et al.[75] used graphene as substrate and Au as catalyst to study the in situ Joule heating-induced evolution of hydrocarbons by passing an electrical current through the substrate. The adsorbed hydrocarbons on top of graphene transformed to atomic monolayer amorphous carbon at around 1000 K and terminated in a completely polycrystalline graphene at temperature exceeding 2000 K.

Furthermore, Liu et al.[88] observed the in situ in-plane growth of graphene at the step-edge of a bilayer graphene substrate, and traced the motion of Si atoms catalyst during graphene growth at the atomic scale using STEM operated at 60 kV. The growth of graphene occurred at 500–700 °C under electron irradiation, with residual hydrocarbons in the imperfect vacuum being used as the carbon source. Si atoms, which acted like catalytic active sites, slid over the graphene edges and were usually pushed to the outermost edges for further growth, or in some cases trapped by defects. They demonstrated that growth orientation was strongly affected by the step-edge structure, and growth speed depended on residual hydrocarbon gas pressure.

B. In situ growth of other 2D materials

The existence of a free-standing crystalline single-atom-thick layer of Fe was demonstrated by Zhao et al.[89] The group used aberration-corrected TEM investigate the structure of 2D Fe membrane, which possessed a square lattice with a 2.65 Å lattice constant at room temperature, as illustrated in Figs. 5(d)–5(f). The holes in graphene were extended to enable Fe atoms and clusters to move into and form a 2D Fe layer. The lattice of Fe layer matched better with armchair edges than zigzag edges in graphene.

Romdhane et al.[90,91] monitored the nucleation and growth of crystalline hexagonally ordered silicon oxide (SiO_2) layers on transition metal surface, such as Fe, ruthenium (Ru), and cobalt (Co) with thickness of 10 nm by in situ TEM [Figs. 5(g) and 5(h)]. The nucleation of silicon oxide often begins at the surface steps[91] or the intersection of planar defects with the metal surface at temperature values above 350 °C.[90] The structural defects in silica possessed the same geometry as polygons from tetragon to nonagon as reconstructed vacancies in graphene layers.[90]

Overall, more detailed investigation into the growth mechanism of 2D materials, such as BN, MoS_2, and WS_2, by in situ TEM, is necessary. The results will help us precisely control the growth of 2D materials for fabrication high-quality materials and tailor them with desired properties for specific applications.

IV. IN SITU NANOFABRICATION

With the rapid development of modern TEM technology, the electron beam can be focused on spots of less than 1 Å in diameter to manipulate and engineer 2D materials at the atomic scale, instead of being used exclusively for imaging. The atoms of 2D materials in

https://doi.org/10.1557/jmr.2015.304 Published online by Cambridge University Press

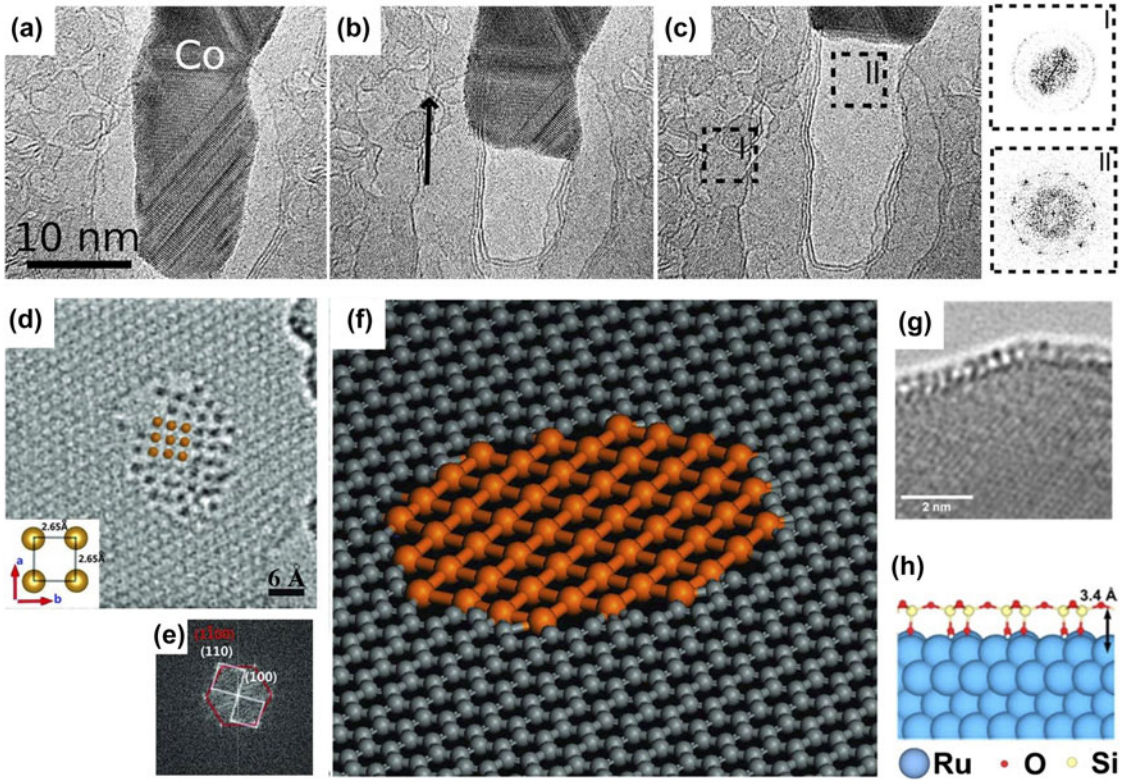


FIG. 5. (a–c) Transformation from amorphous carbon to graphene by tracing the retracting metal lamella. Insets are the diffractograms of the amorphous surrounding film and the graphene layer. Reprinted with permission from Ref. 85, Copyright 2011, American Chemical Society. (d) AC–TEM image of a monoatomic Fe layer with a square unit cell. Inset highlights the interatomic spacing of the square unit cell. (e) Fast Fourier transform of the structure in (d) that shows the lattice relationship between the graphene (red) and the monoatomic Fe layer (white). (f) Schematic models of a suspended monoatomic Fe layer in the graphene pore. Reprinted with permission from Ref. 89, Copyright 2014, American Association for the Advancement of Science. (g) Side view of the SiO_2 cellular structure on Fe at 470 °C. The height of the cells is approximately 0.4 nm. (h) Schematic models of a SiO_2 structure on Ru. Reprinted with permission from Ref. 90, Copyright 2013, American Chemical Society.

specific regions will be sputtered by the focused beam, during which the electron energy is higher than the threshold energy for atomic displacement. Nanofabrication strongly depended on the irradiation time and beam conditions, including beam size, brightness, and electron energy.

A. Doped 2D materials

Functionalized 2D materials are doped to tailor their properties for dedicated applications, including gas sensors, superconductors, supercapacitors, nanoelectronics, and spintronics. We can use the focused electron beam in TEM to create atomic-scale defects and fill these defects with the required dopants.

Different elements including Pt,[58,92,93] Co,[58] Au,[92,93] Mo,[94] W,[95] Fe,[57,96] and Si,[97,98] have been successfully doped in graphene by in situ TEM. Foreign atoms rapidly diffuse under electron irradiation and can be trapped in beam-induced vacancies. Most foreign atoms are located slightly outwards from the graphene layer because of the larger atomic radii of these atoms.[99] The high binding energy between carbon and foreign atoms ensures the stability of vacancy-dopant complexes, and foreign atoms are difficult to be removed by thermal excitation or electron irradiation.[58,92,94] Nevertheless, reconstructed defects with pentagonal, heptagonal or larger rings acting as trapping centers present lower binding energy and may result in detrapping[94] and migration[92,95] of foreign atoms at high temperatures levels or high beam current densities. Figures 6(a)–6(h) show long-distance jumps of a W atom on a few-layer graphene sheet at 470 °C and an electron-beam current density of 110 A/cm^2.[95] A W atom oscillates between two reconstructed defects with a distance of 0.5–1.4 nm, as shown in Figs. 6(i)–6(l). The strain field around reconstructed defects can result in attraction between defect and adatom.[95]

A Fe atom can occupy a MV in the graphene sheet as substitutional impurity or replace two carbon atoms in a DV as interstitial impurity, as shown in Figs. 7(a)–7(d).[57] The Fe atoms that occupied MV and DV are expected to possess high stability because of the high binding energy between carbon and metal atoms mentioned above. However, as revealed in Figs. 7(e)–7(t), Fe atoms can migrate under electron irradiation, the reason

https://doi.org/10.1557/jmr.2015.304 Published online by Cambridge University Press

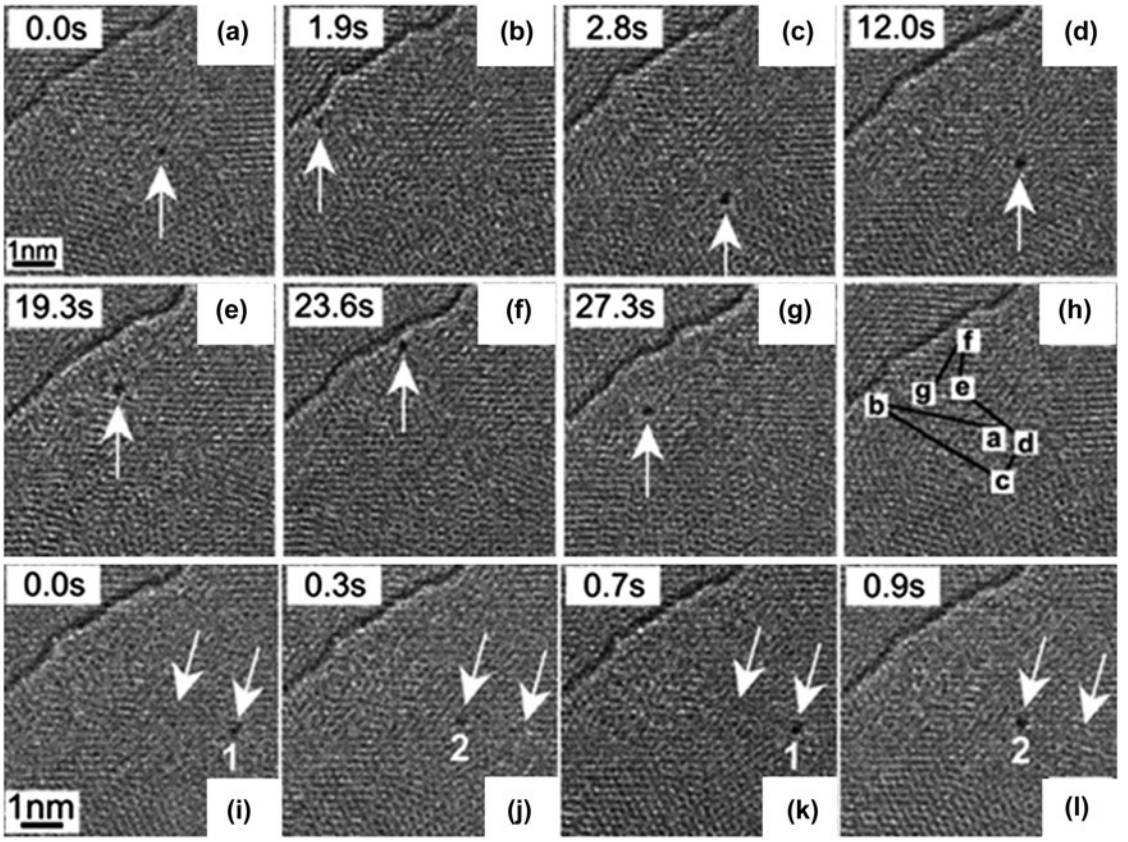


FIG. 6. (a–g) W atom migration (arrowed) on a few-layer graphene sheet at 470 °C. (h) Entire path from (a) to (g). (i–l) Back-and-forth jumping of a W atom between two trapping centers, 1 and 2 (arrowed). Reprinted with permission from Ref. 95, Copyright 2010, American Physical Society.

may be the instability of carbon atoms surrounding the Fe atom under electron irradiation, which indirectly induce the perturbation of Fe.[57] In details, Figs. 7(e)–7(h) show a Fe atom shifts between adjacent MV sites; Figs. 7(i)–7(l) show a Fe rotation through a change in the DV sites, whereas Figs. 7(m)–7(p) to Figs. 7(q)–7(t) illustrate a Fe atom switching between MV and DV sites. Furthermore, under continuous electron irradiation, the single Fe dopant will also be active and attract a second Fe atom to be trapped to form a Fe dimer.[96] As shown in Figs. 7(u)–7(x), the four different stable structures are as follows: two variants of Fe dimer in a graphene trivacancy, an Fe dimer embedded in two adjacent MVs, and an Fe dimer trapped in a tetravacancy.[96] Not only single or double foreign atoms can be captured by a graphene nanopore, but also atom clusters, such as Si_6, as demonstrated by Lee et al.[98]

Compared with the stable vacancy-dopant complex in lattice, graphene edge can act as trapping sites for single atom as well as exhibit a rich dynamic behavior.[93,100] Wang et al.[93] observed an Au atom migration along the graphene edge via TEM operated at 60 kV. Notably, the trapping and detrapping processes of Au are cooperative motions with surrounding carbon atoms, especially those with unsaturated bonds.[93] The trapped atom at the edge can provide a catalytic sites for the carbon atom dissociation from graphene, whereas the trapped atom itself is intact.[100] Wang et al.[100] found that the Si adatom lowers the binding energy of surrounding carbon atoms and eases their removal from graphene edges under electron irradiation.

Electron-beam-induced doping can be applied in carbon atoms substitution of boron and nitrogen in h-BN to tune the electrical and magnetic properties of h-BN with different carbon content.[101] Wei et al.[101] put a paraffin wax several millimeters away from h-BN on the TEM grid as a carbon feedstock, the boron and nitrogen atoms were sputtered by electron beam (acceleration voltage at 300 kV) and left vacancies, which acted as attractive sites for carbon atoms to incorporation. They successfully transformed h-BN from electrical insulators to conductors through carbon substitutions.[101] In theory, the physical properties of MoS_2 and other TMDs can also be modified by doping different foreign atoms.[32,83] The filling of the electron beam-induced vacancies in MoS_2 was demonstrated to be feasible, but the impurity type cannot be easily identified by TEM.[32] Therefore, further investigations on doped 2D materials and how foreign atoms tune their properties are needed to carry out.

https://doi.org/10.1557/jmr.2015.304 Published online by Cambridge University Press

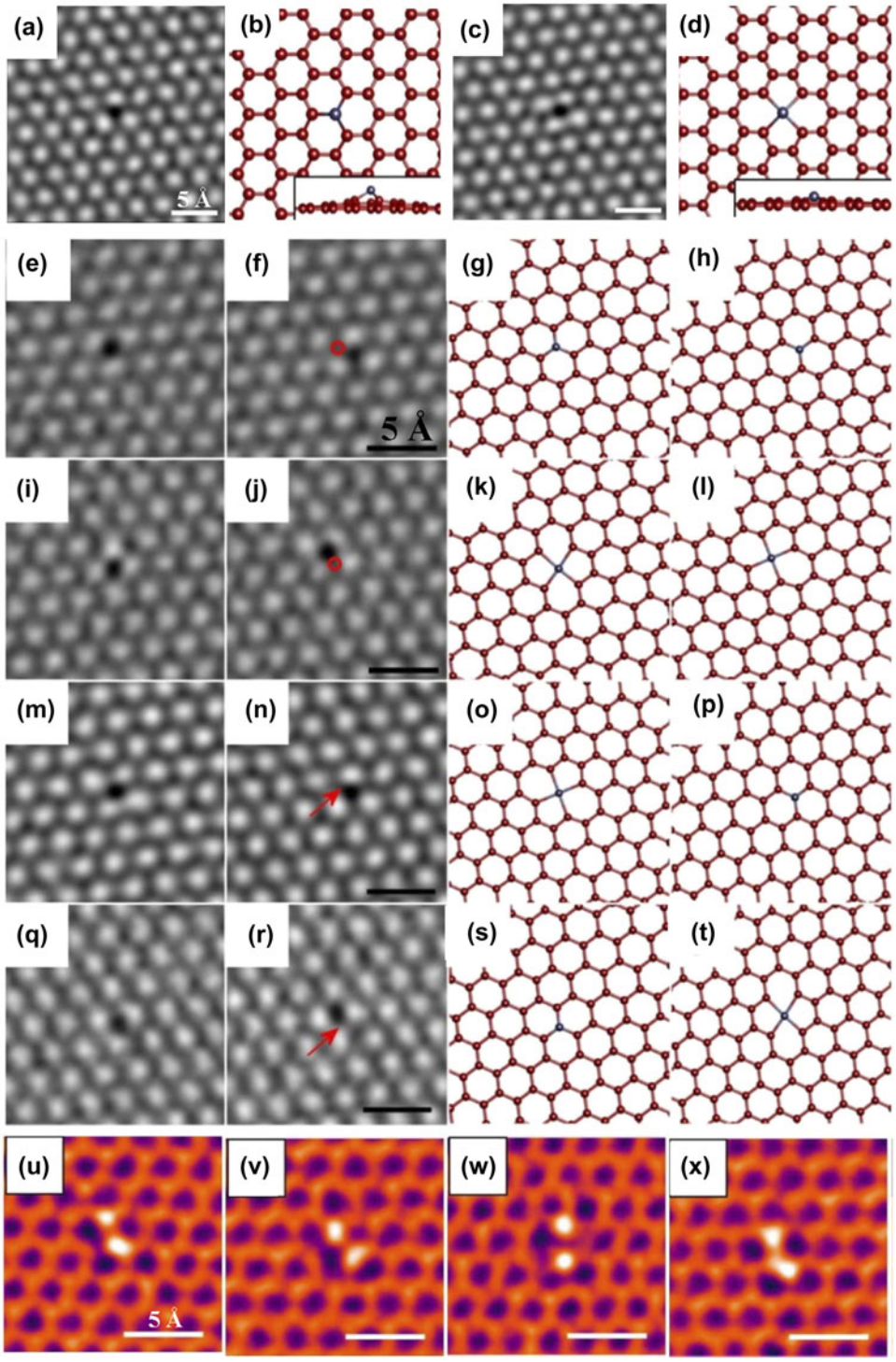


FIG. 7. Smoothed AC–TEM image of (a) an Fe substitutional defect in a graphene MV and (c) an Fe interstitial defect occupying a DV, (b) and (d) are the corresponding atomic models (the inset shows a side view). (e–t) AC–TEM images of defective Fe atom mobility and corresponding atomic models. (e and f) Shifting between adjacent MV sites, (g and h) atomic models. (i and j) Changing between two DV sites, (k and l) atomic models. (m and n) Switching from a DV to an MV site, (o and p) atomic models. (q and r) Moving from an MV to a DV site, (s and t) atomic models. Red annotations (circles or arrows) show the location of the defective atom in the previous frame. The accompanying atomic models show the Fe adatom in blue. Reprinted with permission from Ref. 57, Copyright 2013, American Chemical Society. (u–x) Smoothed AC–TEM images of Fe dimers in graphene vacancies. A pair of Fe atoms in (u) trivacancy, (v) alternative trivacancy, (w) tetravacancy, and (x) two adjacent monovacancies. Reprinted with permission from Ref. 96, Copyright 2014, American Chemical Society.

https://doi.org/10.1557/jmr.2015.304 Published online by Cambridge University Press

Electron beam-induced doping is a well-controlled and simple strategy, as well as can cause less damage and can be performed at room temperature. Given these characteristics, different 2D material defects can be patterned through an electron beam and subsequently trapped or assembled foreign atoms of specific sizes or properties inside them, which may potentially lead to practical applications in the future.

B. Nanopores

Solid-state nanopores embedded in a thin membrane open up a new field of nanosensors for their small response time and single molecule precision of characterization of chemicals and biomolecules, which may especially have revolutionary impacts on realizing single molecular gene sequencing.[102,103] The focused electron beam can be used to fabricate nanopores in silicon nitride,[104] silicon oxide,[102] graphene[103,105] and magnesium (Mg)[106,107] in TEM. However, electron beam does not give full control over the nanopores at the nanometer scale because no images can be recorded during drilling. Nanopore size and crystallinity can be further fine-tuned by electron irradiation[102,106,107] and in situ thermal heating.[103,108] Nanopore sizes have been demonstrated to be reduced or increased to find a configuration with the lowest surface-free energy. Whether the nanopores expand or shrink depends on the relationship between sheet thickness and nanopore diameter.[102,103] In detail, the nanopores with diameter smaller than thickness will lower the surface-free energy by reducing size, whereas the nanopores with diameter larger than thickness will do so by increasing size.[102] The contraction rate of the nanopores is inversely proportional to the membrane thickness; when the membrane is thinner, the contraction rate is larger.[104]

Figures 8(a)–8(c) illustrate the electron beam induced nanofabrication on a graphene membrane. Figure 8(a) is the pristine graphene membrane before high dose irradiation. After long time exposure to electron beam, the region highlighted by dashed rings transformed into amorphous carbon in Fig. 8(b) and eventually formed a nanopore in Fig. 8(c). The graphene nanopores open up new avenues for the single-base resolution on DNA because the distance between adjacent base pairs on stretched DNA (0.36 nm) matches well with the single-layer graphene thickness (0.34 nm).[103] As shown in Figs. 8(d)–8(g), electron irradiation induced the silicon oxide nanopore to gradually shrink from 19 to about 3 nm.[102]

Furthermore, the nanopores can also nucleate at contamination sites[47] or surrounding vacancies[109] without the focused electron beam.

C. Nanoribbons

Under electron irradiation, the two adjacent graphene nanopores are continuously growing and the bridges between them narrowed to nanoribbons.[108,110–112] Graphene nanoribbons open up a band gap in graphene and can exhibit either quasimetallic or semiconducting behavior, which highly relies on the edge structure.[113] For instance, the graphene nanoribbons with a higher zigzag edge fraction exhibited a smaller energy gap than predominant armchair nanoribbons of similar width.[114] Therefore, controlling the configuration and crystallinity of the edge structures is important to tailor the properties

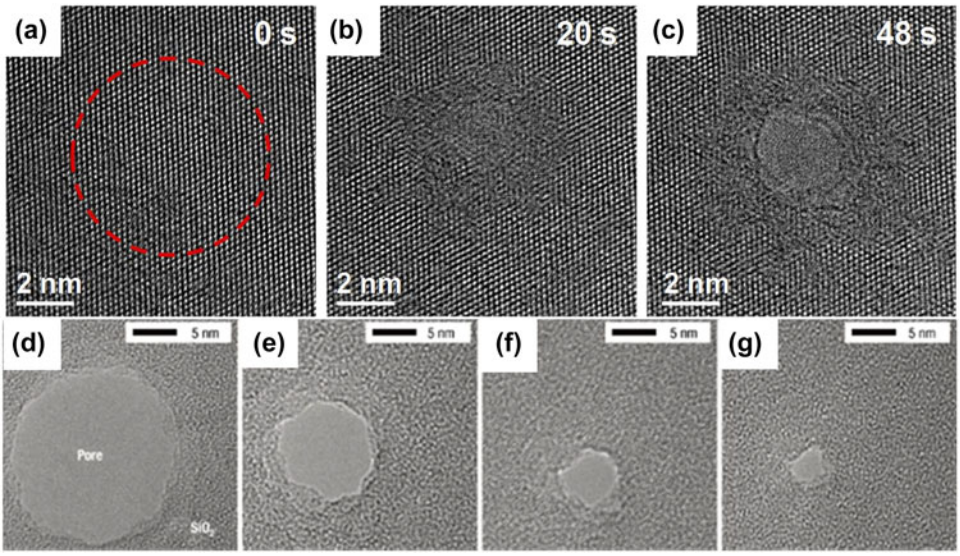


FIG. 8. (a–c) Nanopore fabrication in the graphene sheet. (a) Pristine graphene membrane before high-dose irradiation. The dashed ring highlights the region to be irradiated. (b–c) The same region in (a) after electron beam irradiation for 20 and 48 s and eventually forming a graphene nanopore. Reprinted with permission from Ref. 105, Copyright 2014, Wiley–VCH Verlag GmbH & Co. KGaA, Weinheim. (d–g) The shrinkage process of a SiO_2 nanopore from a size of 19 to about 3 nm under electron beam irradiation. Reprinted with permission from Ref. 102, Copyright 2003, Nature Publishing Group.

https://doi.org/10.1557/jmr.2015.304 Published online by Cambridge University Press

of nanoribbons. Jia et al.[113] produced atomically smooth and highly crystalline zigzag or armchair edges from defective nanoribbon edges by using Joule heating and electron irradiation.

When the graphene nanoribbon width is reduced below 1 nm, it reconstructs from the hexagonal structure to intermediate structures with pentagons and heptagons.[110] Eventually, the graphene nanoribbons convert to one or two atomic carbon chains.[108,110,111] The double chains are generally shorter than the single carbon chains, whereas the single chains frequently change their anchor sites.[108,111] The thinning process is dominated by a surface atom sputtering mechanism, in which the atoms at the edges are preferred to be removed.[111] Moreover, monoatomic carbon chains could be fabricated from graphene nanoribbons through loading a bias by Cretu et al.,[115] and they measured the in situ electrical properties and found that the electrical conductivity of atomic carbon chains is lower than predicted ideal chains. For TMDs, such as MoS_2, $MoSe_2$, WS_2, and WSe_2, the nanoribbons with sub-nanometer width can be widely formed between holes created by manipulating a focused electron beam.[16,17] Liu et al.[17] combined the in situ HRTEM characterization with first-principle calculations and demonstrated the sub–1 nm ribbon as a Mo_5S_4 crystal with a band gap of 0.77 eV, which indicates the nanoribbon is semiconducting [Figs. 9(a)–9(f)]. On the other hand, Lin et al.[16] gave a more detailed investigation of nanoribbon structure and property through STEM and in situ electrical measurement. The nanoribbons with stoichiometry MS (M = Mo or W, X = S or Se) matched better with the experimental results and were demonstrated to be metallic [Figs. 9(g)–9(n)]. The nanoribbons are mechanically robust and have high crystalline perfection,[16,17] which may serve as interconnects in future flexible nanocircuits.

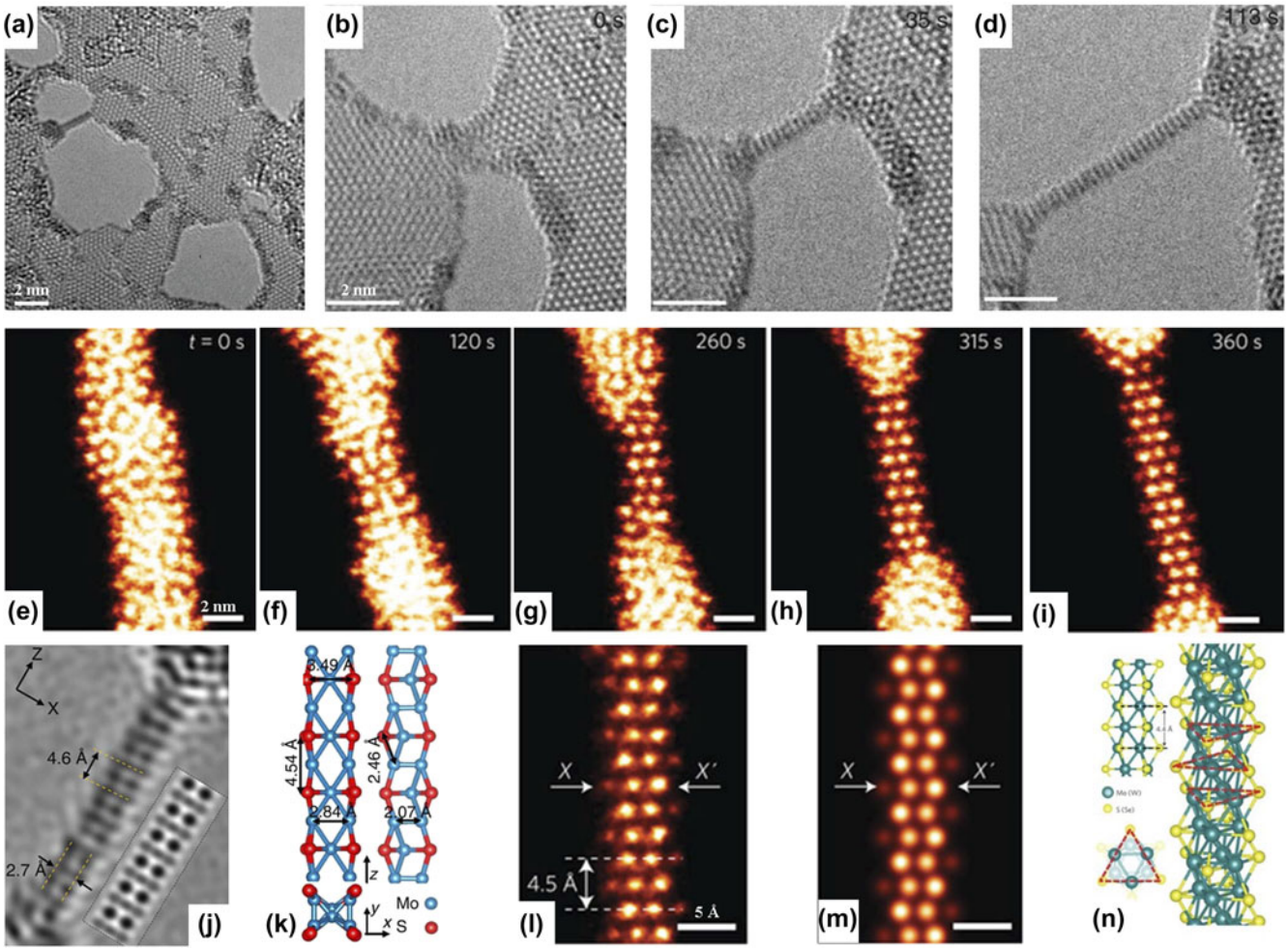


FIG. 9. (a–d) TEM images of Mo_5S_4 nanoribbon formation. The bridge between two adjacent nanopores narrowed to nanoribbons with nanopore expansion. (e–i) False-colored STEM images of the MoSe nanoribbon formation. (j) HRTEM image and simulated TEM image (labeled by the dotted rectangle) of Mo_5S_4. (k) Three-view depictions of the Mo_5S_4 nanoribbon. (l) STEM image and (m) simulated STEM image of MoSe nanoribbon. (n) Atomic structural model of the MS (M = Mo or W, X = S or Se) nanoribbon. (a–d and j–k) Reprinted with permission from Ref. 17, Copyright 2013, Macmillan Publishers Limited. (e–i and l–n) Reprinted with permission from Ref. 16, Copyright 2014, Macmillan Publishers Limited.

https://doi.org/10.1557/jmr.2015.304 Published online by Cambridge University Press

The approach in sculpting 2D materials into nanopores, nanoribbons, and nanochains by electron irradiation could be developed into a general controllable method for ultrasmall component fabrication for future functional devices.

V. IN SITU PROPERTY CHARACTERIZATION

Given a clear understanding of 2D material structures at atomic resolution, introducing external fields, such as electron irradiation, thermal excitation, electrical field, and mechanical force, into TEM is significant in the investigation of essential structural evolution and structure–property relationship of 2D materials in real environment. Various external stimuli can be recognized through different specimen holders.

A. Electron irradiation

Electron irradiation is inevitable and can be easily recognized in TEM. A virtue can be made out of necessity, and electron irradiation can not only induce in situ growth and nanofabrication of 2D materials by using high temperature, as discussed above, but also induce structural evolution such as production,[14,24,48] migration,[49] reconstruction, and annihilation[14,24] of defects. Modern HRTEM with ultrafast imaging technology makes it possible to record the dynamic process of structural evolution in real time, which leads us to a new understanding of electron irradiation effects in 2D materials.

Robertson et al.[24] utilized the focused electron beam to generate defects in graphene layers, and investigated how the beam current density and exposure time influence the complexity of defects. They found that defects were created in a clean area ($\sim 10 \times 10$ nm^2) of pristine graphene only when the beam current density reached $\sim 10^8$ e/m^2 s^1, and increasing the exposure time (up to 120 s) to the focused beam gave rise to further complex defects.

The full life cycle of a dislocation from generation, migration, interaction with other dislocations to eventual annihilation under electron irradiation has been recorded

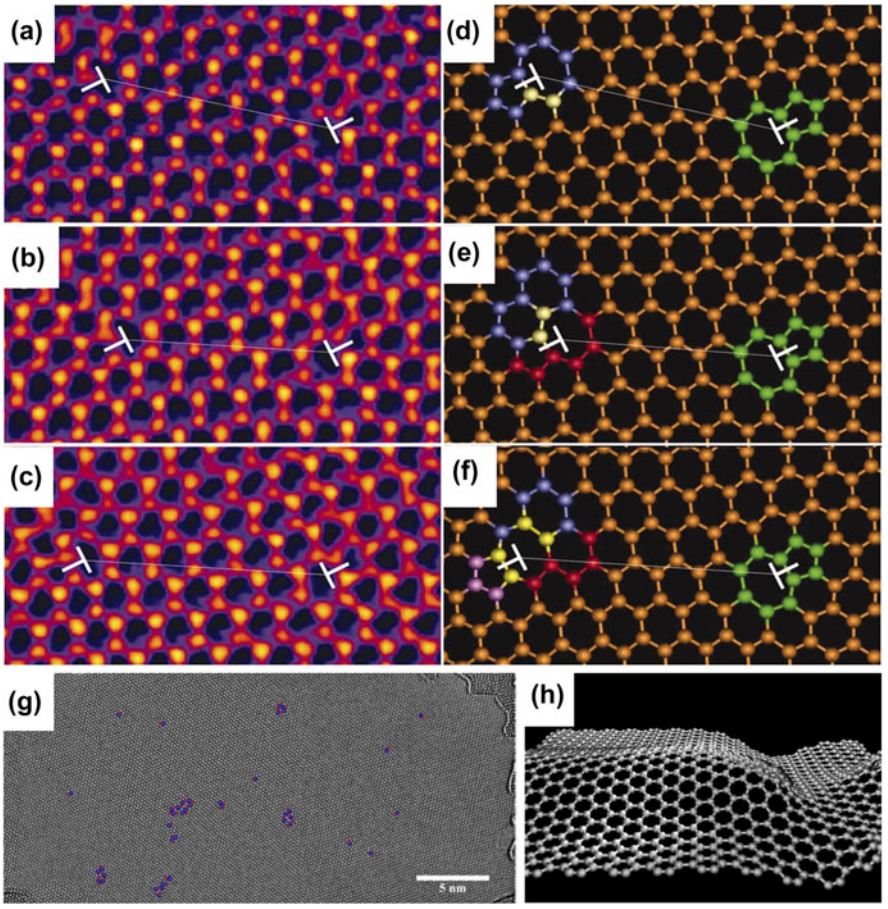


FIG. 10. (a–c) Real-time dislocation dynamics: HRTEM images showing changes in the position of an edge glide dislocation with time under continuous electron beam irradiation. (a) Time = 0 s, (b) time = 141 s, and (c) time = 321 s. (d–f) Atomic models of (a–c), respectively. White T indicates the position of dislocation. Reprinted with permission from Ref. 15, Copyright 2012, American Association for the Advancement of Science. (g) TEM image of 41 dislocations [5–7 ring pairs (red−blue)] in graphene introduced by electron beam irradiation. (h) Schematic ripple morphology in graphene. Reprinted with permission from Ref. 116, Copyright 2013, American Chemical Society.

https://doi.org/10.1557/jmr.2015.304 Published online by Cambridge University Press

by Lehtinen et al.[13] At first, carbon atoms were sputtered by electron beam and formed vacancies in graphene, and the vacancies agglomerated and reconstructed into a dislocation under continuous electron irradiation.[115] Subsequently, the dislocation migrated within the graphene sheet through bond rotations along the glide plane (glide) and two carbon atom addition or removal (climb) in different directions.[115] The mechanism of migration through beam-driven bond rotations was consistent with what Kotakoski et al.[49] found through observation of DV motion in graphene using STEM operated at 60 kV. Eventually, due to the attractive force between the dislocations and the migration induced by electron irradiation, they moved toward each other and ultimately annihilated.[115] On the other hand, dislocations in graphene can generate in-plane strain[15] and out-of-plane distortions and ripples. Warner et al.[15] studied the dynamics of dislocation pairs in graphene and their

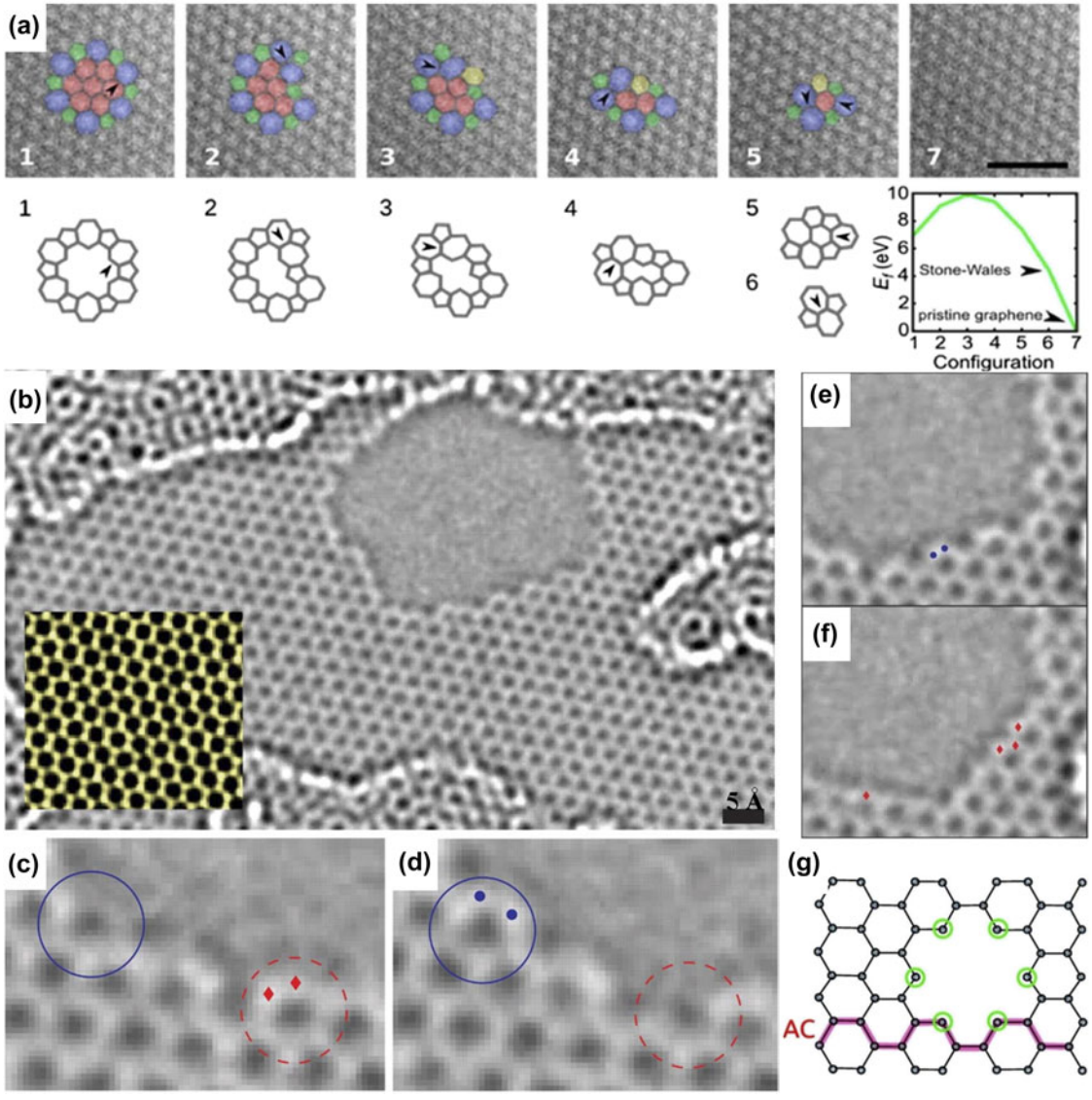


FIG. 11. (a) Disappearance process of a flower defect under electron beam irradiation during a 30 s total exposure, below the experimental images are DFT-optimized models of the corresponding structures above and a plot of their formation energies. Rotating bonds are indicated by black arrows. Reprinted with permission from Ref. 66, Copyright 2012, American Chemical Society. (b) AC–TEM image of a hole in a single layer of graphene produced by prolonged irradiation, (Inset) Averaged series of images showing the atomically resolved graphene lattice. (c–d) Hole evolution, with (d) following 4 s after (c). Two carbon atoms (red dots in the dashed circle) are removed while two nearby carbon atoms (blue dots) bind to their neighbors to close a hexagon (solid circle). (e–f) Edge reconfiguration: conversion from an armchair edge (b) to a zigzag edge (c) after 4 s. The two atoms marked as blue dots in (e) disappeared in (f), where four new carbon atoms are incorporated as red diamonds. Reprinted with permission from Ref. 10, Copyright 2009, American Association for the Advancement of Science. (g) Schematic morphology of the hole in graphene. Under-coordinated atoms, which are equally likely to be sputtered away marked with green circles. Removing any of these atoms results in zigzag edges. Reprinted with permission from Ref. 68, Copyright 2012, American Chemical Society.

https://doi.org/10.1557/jmr.2015.304 Published online by Cambridge University Press

impact on the lattice structure of graphene. Figures 10(a)–10(f) show the dislocations migrate along the zigzag lattice through glide and climb mechanism activated by electron beam, which was mentioned above.[115] They used the geometric phase analysis to map the strain fields, and illustrated that the graphene was deformed by bond compression or elongation, shear strain and lattice rotations of dislocations.[15] Moreover, Warner et al.[116] utilized a novel approach to introducing a large number of dislocations (5–7 ring pairs) in a well-defined graphene area by slowly raster-scanning a focused electron beam back and forth. To release the large strain produced by the large amount of dislocations, the graphene formed out-of-plane distortions and ripples, as shown in Figs. 10(h).[116] The rippling was dynamic and could fluctuate between various structural configurations under electron irradiation, which was distinct from in-plane lattice compression mentioned above.[15]

The grain boundary migration in graphene with atomic resolution has been investigated in real time by using electron irradiation-induced bond rotation in aberration-corrected TEM.[66] The grain boundary translation only occurs at significant high boundary curvature, which has a high driving force.[66] Figure 11(a) step-by-step shows how a flower-like grain boundary unwinds under electron irradiation and ultimately disappears, resulting to pristine graphene restoration. Moreover, each of the unwinding steps lowers the total system energy, and the process is irreversible.

The carbon atoms dynamics at the edge of a hole in single-layer graphene under electron irradiation is recorded by using the aberration corrected TEM equipped with a monochromator.[10] The hole formed by prolonged electron irradiation is showed in Fig. 11(b) at atomic resolution. The disappearance of two carbon atoms (red dots) and the incorporation of two atoms (blue dots), with time interval of 4 s, can be seen in Figs. 11(c) and 11(d). An armchair sequence at a corner transformed into a zigzag sequence over the course of 4 s, as shown in Figs. 11(e) and 11(f). The three main competing mechanisms that result in the dynamics of edge reconstruction and hole growth are the migration of dangling carbon atom, the ejection of carbon atom along the edge, and the addition of carbon atoms from adsorbates attached on the hole.[10]

Understanding the evolution and dynamics of dislocations, grain boundaries and edge structures under electron irradiation, represents a significant step forward in realizing the goals to manipulate and modify of carbon nanomaterials by utilizing the electron beam for nanodevice fabrication in the future.

B. Thermal field

In situ heating can be realized by placing a heating element at the tip of a TEM specimen holder, and the temperature is set using an external controller. The three typical types of in situ heating TEM holders are furnace-heating holders, wire-heating holders, and

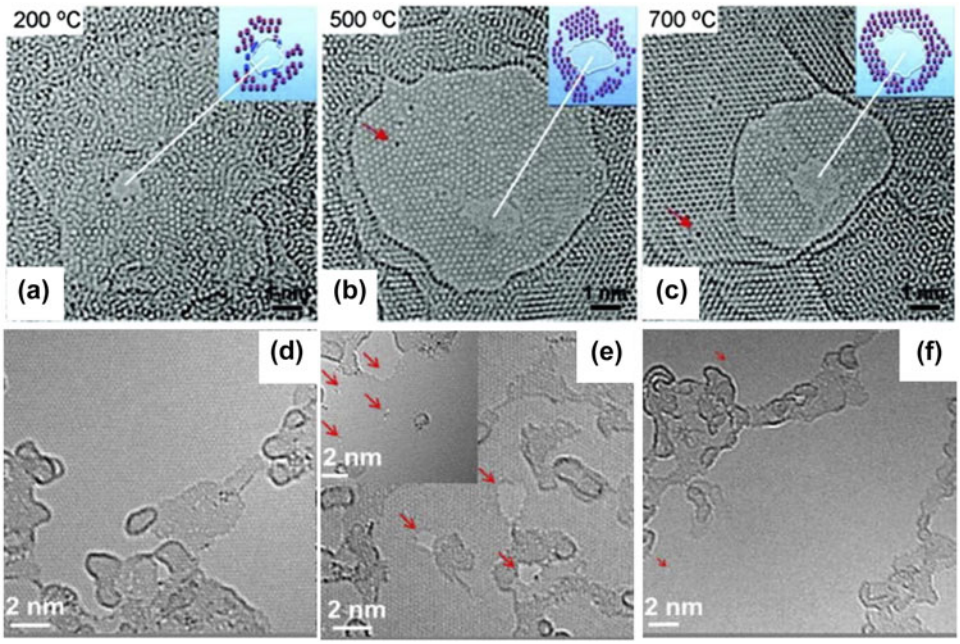


FIG. 12. (a–c) Self-repair process of the graphene nanopore from (a) amorphous to (b) polycrystalline, and ultimately to (c) single crystalline with the temperature increasing from 200 to 500 °C, and finally to 700 °C. Reprinted with permission from Ref. 108, Copyright 2011, American Chemical Society. (d–f) HRTEM images of three graphene samples: (d) pristine, (e) after 5 s of plasma treatment, and (f) after annealing at 750 °C. The surfaces are partially covered by polymethyl methacrylate (PMMA) residue. Red arrows indicate honeycomb lattice vacancies. Reprinted with permission from Ref. 117, Copyright 2013, American Institute of Physics.

https://doi.org/10.1557/jmr.2015.304 Published online by Cambridge University Press

membrane-heating holders.[18] In furnace-heating holders, the thermal expansion effect causes a serious problem of sample drifting when changing temperature, which makes it impossible to take HRTEM images in a short period of time.[18] A cooling system is required to maintain the stability of the holders because the heating area is large. The wire-heating holder can reach a temperature as high as 1500 °C and do not need cooling water, whereas the membrane-heating holder has the fastest temperature change, ranging at 10^6 °C/s.[18] However, sample drifting cannot be avoided. An alternative approach is to use the Joule heating with small specimen drift when a bias voltage is applied to an STM or electrical bias holder. Unfortunately, the temperature induced by Joule heating cannot be directly read. All these heating methods make it feasible to study thermal properties of 2D materials as well as thermal excitation-induced behavior.

As mentioned above, at elevated temperatures, nanopores can shrink or expand,[103,108] foreign atoms can be introduced into 2D materials to tune their properties,[92,94,95] and thermal-induced in situ growth of graphene can also be realized in TEM.[75,85,86,90,91]

2D material defects are usually undesirable for electronic applications; thus, repairing the defects would be extremely useful. Some defects can relax to simple structures through bond rotations and surface adatom incorporations under electron irradiation.[24] However, this process may take a long time and is infeasible for large-scale graphene restoration. Fortunately, at high temperatures, the diffusing carbon adatoms can be rapidly trapped by defects, which results in self-healing and single-crystallinity recovery of graphene.[108,117] Figures 12(a)–12(c) reveal a temperature-dependent self-healing mechanism that tunes the graphene nanopore from amorphous to single crystalline at temperature of 700 °C.[108] Figures 12(d)–12(f) show HRTEM images of the three graphene samples before and after plasma treatment and after annealing.[117] After plasma treatment, a large amount of vacancies exists in graphene, which are indicated by red arrows in Fig. 12(e). As shown in Fig. 12(f), the defect density is substantially reduced after annealing at 750 °C.

Moreover, thermal excitation can induce phase transition,[118,119] as shown in Fig. 13. Monolayer MoS_2 has two distinct symmetries: the semiconducting 2H (trigonal prismatic D_{3h}) and the metallic 1T (octahedral O_h). The dynamic transformation process between 2H and 1T phases with atomic resolution was first investigated using in situ STEM by Lin et al.[120] Phase transformation occurred at 600 °C under continuous electron irradiation by gliding atomic planes of S and Mo. Phase transition requires an intermediate phase (α-phase) and migration of two kinds of boundaries (β- and γ-boundaries), as shown in Figs. 13(c)–13(e). The α-phase is a precursor during phase transition, which consists of 3–4 constricted MoS_2 zigzag chains.[119] The β-boundary contains four-membered Mo–S rings, whereas the γ-boundary includes two constricted MoS_2 zigzag chains.[119] The coexistence of the semiconducting 2H and the metallic 1T phase can form the coherent electronic heterostructures with tunable band gap, which may be exploited for novel molecular functionalities in the future.[119,120]

By in situ Joule heating, graphene cracks propagate from the flake edges and result in the formation of narrow gap before breakdown.[121,122] In another example, in situ Joule heating can induce the suspended few-layer graphene to sublimate, with the sublimation fronts predominantly consisted of zigzag edges.[123] The graphene edges reconstructed during sublimation and most frequently formed bilayer edges, indicating that bilayer edges are more stable than monolayer at high temperatures.[123]

C. Electrical field

In situ electrical measurement is often used to study behavior and structural changes[121,123] of specimens in an electrical field, electrical transport properties[16,115] of nanostructures. STM holders are popular for these application purposes. A metallic probe in the STM holder is present, which connects to the power supply unit and can

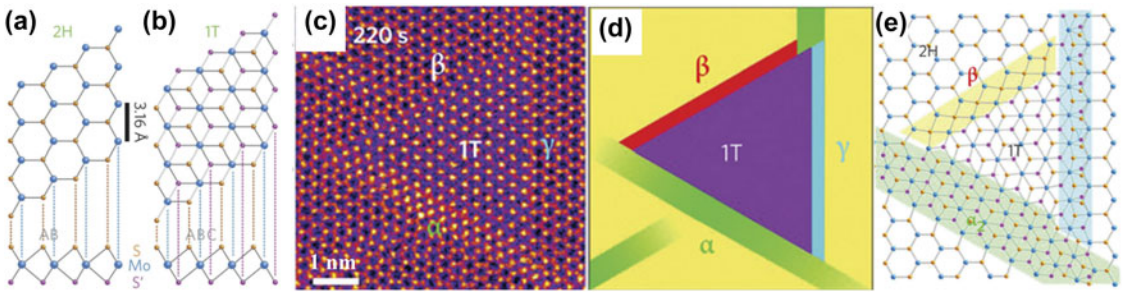


FIG. 13. (a–b) Schematic models of monolayer MoS_2 with 2H (a) and 1T (b) phases in basal plane and cross-section views. Mo, blue; top S, orange; bottom S′, purple. (c) STEM high angle annular dark field (STEM-HAADF) image of triangular 1T phase MoS_2 embedded in 2H phase MoS_2. At the edges between the 1T and 2H phase are the three different boundaries (α, β, and γ). (d) Simple schematic illustration and (e) schematic model of (c). Reprinted with permission from Ref. 119, Copyright 2014, Macmillan Publishers Limited.

https://doi.org/10.1557/jmr.2015.304 Published online by Cambridge University Press

move back and forth in fine steps controlled by a piezo manipulator.[18] Different kinds of tips, such as W, Cu, Au, and Ag, are placed on the probe to contact the specimens. A circuit can be formed with the TEM specimen and probe for electrical current to pass through. For example, in situ electrical measurement of MoSe nanowire provides direct evidence of the conversion from semiconducting monolayer to metallic nanowire.[16]

With in situ TEM, Barreiro et al.[121,122] observed how the current modified the graphene structure and vice versa. Figure 14(a) schematically shows the in situ TEM setup with a sheet of few-layered graphene linked with two free-standing gold electrodes to form a circuit. Through large bias application, few-layered suspended graphene were peeled off layer by layer until only a single layer remained.[121] Subsequently, the monolayer graphene began to crack and formed a narrow constriction.[122,123] By real-time electrical measurement, the current through the constriction drops when the constriction width is reduced, and eventually drops to zero when the constriction fails [Fig. 14(b)]. Current drop means the resistance is increasing, which indirectly proves that the carbon atoms are sublimed under the large bias.[121,122]

Furthermore, Lu et al.[125] found that the graphene constriction conductance was high and approximately varied with width, as $G(w) = (e^2/h)\, w^{0.75}$, where w is the constriction width in nanometers. When the graphene nanoconstriction is narrowed to single carbon atom chains, a characteristic drop of the electrical current occurs, as shown in Figs. 14(c) and 14(d).[115] For the electrical measurements of monoatomic carbon chains, Torre et al.[124] found that the strained carbon chains were semiconducting with polyyne structure (–C≡C–C≡C–C≡), while unstrained chains were metallic with cumulene

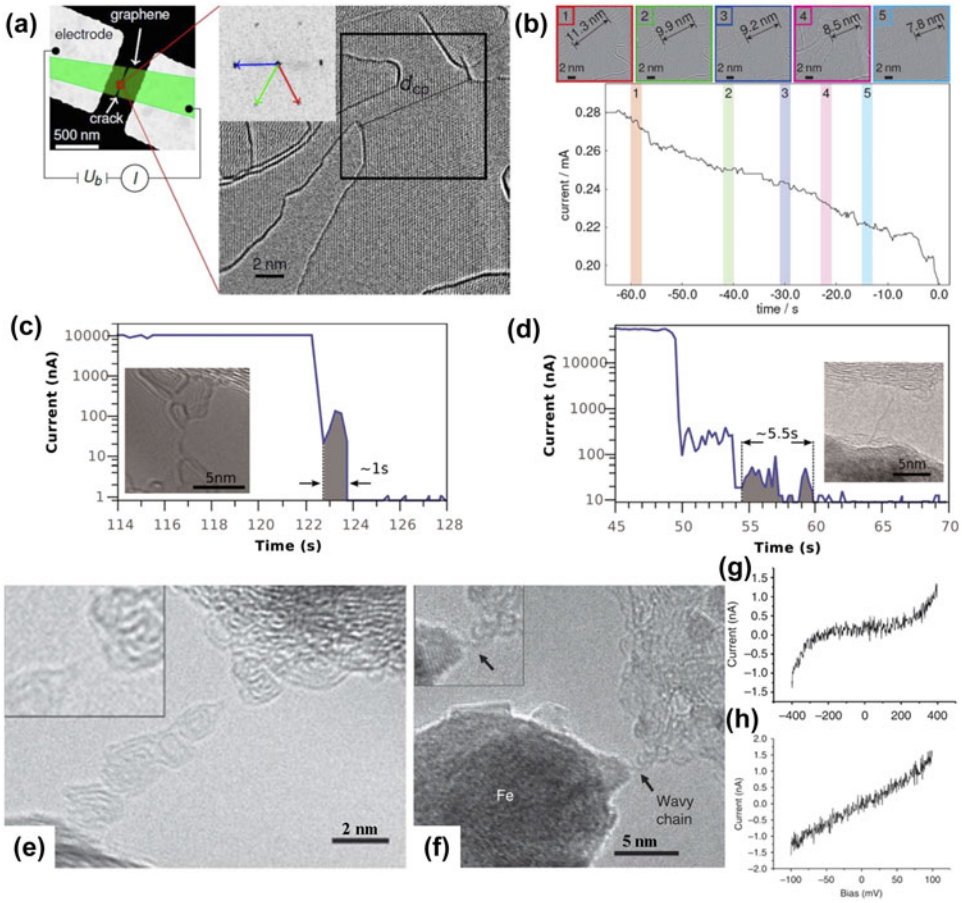


FIG. 14. (a) Schematic overview of the setup. (left) STEM image of the electrodes with a sketch of an overlying graphene ribbon with a central constriction. (right) TEM image of the bilayer graphene constriction at high bias. The inset is the FFT of the marked region in the micrograph. (b) Series of micrographs at high bias. The plot indicates the measured current through the constriction. The transparent bars indicate when the respective series of color-coded micrographs were taken. Reprinted with permission from Ref. 122, Copyright 2012, American Chemical Society. (c–d) Electrical current through two monatomic carbon chains at a constant bias of 1 V. Blue curve shows the evolution of the current. The filled regions under the curve correspond to the periods where the chains appeared. The image insets show the respective chains. Reprinted with permission from Ref. 115, Copyright 2013, American Chemical Society. (e) TEM images of a strained carbon chain and (g) corresponding current–voltage curves. (f) TEM images of an unstrained wavy carbon chain and (h) corresponding current–voltage curves. Reprinted with permission from Ref. 124, Copyright 2015, Macmillan Publishers Limited.

https://doi.org/10.1557/jmr.2015.304 Published online by Cambridge University Press

structure (=C=C=C=C=C=). They also observed the semiconductor–metal transition of carbon chain through a release of strain. The S-shaped current–voltage curve in Fig. 14(g) indicates the semiconducting behavior of carbon chain under strain.[124] Conversely, an unstrained chain is shown in Fig. 14(h), in which the current–voltage curve is a linear.[124]

D. Mechanical force field

When the materials size decreases to the nanometer level, the mechanical properties, including strength, hardness, and toughness, may experience dramatically changes.[18] Predicting and correctly understanding nanostructure failure is important, as well as the material size effect on mechanical behaviors.[18] Therefore, mechanical TEM holders are designed to load a tensile or compressive mechanical force on TEM specimens and track the structural evolution simultaneously.[18]

The mechanical properties of CNTs,[126] nanocrystals,[127–129] and nanowires[130–133] have been investigated in detail by in situ mechanical techniques. However, given the nature of 2D materials, the boundary conditions are complicated and more difficult to control in in situ experiment. The mechanical properties of 2D materials are still difficult to characterize inside a TEM.

Tang et al.[134] developed an in situ TEM probing technique to investigate the nanomechanical cleavage of 2D crystals. The MoS_2 was successfully cleaved from a monolayer to double layers and up to 23 atomic layers, which demonstrated that the technique could realize layer number selective cleavage, and such cleavage is highly reversible.[134] The MoS_2 crystals were loaded on the Au stage and a W tip was controlled to cleave and bend the MoS_2 atomic layers, as shown in the schematic [Fig. 15(a)] and corresponding TEM image [Fig. 15(b)]. Figures 15(c)–15(f) show the cleavage process of a monolayer MoS_2. The W probe initially contacted the outermost monolayer edge and then moved at an inclined angle marked by a black arrow, which made the monolayer MoS_2 attach to the probe [Fig. 15(c)]. By moving the probe away, the monolayer MoS_2 flake was stretched and eventually detached from the crystal.[134]

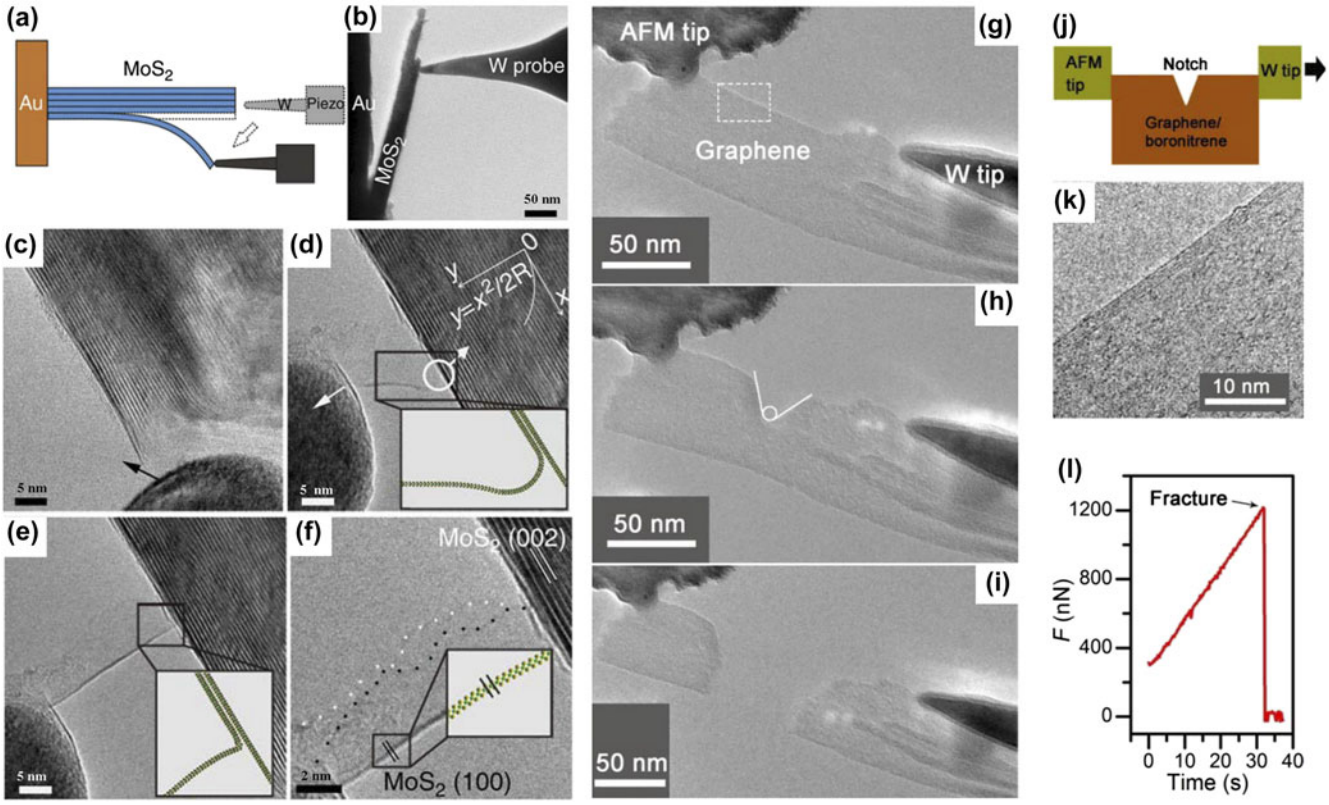


FIG. 15. (a) Schematic of the experimental setup and (b) corresponding TEM image. (c–f) Nanomechanical cleavage process of a monolayer MoS_2: (c) the initial contact, (d) intermediate peeled-off and bent, and (e) stretched states of a monolayer MoS_2. (f) HRTEM image of the cleaved monolayer MoS_2, revealing the (100) atomic stacking order, as well as the MoS_2 (002) lattice fringes of the "mother" crystal. Reprinted with permission from Ref. 134, Copyright 2014, Macmillan Publishers Limited. (g) TEM image of a multilayer graphene nanosheet clamped between the atomic force microscope (AFM) and W tips. (h) TEM image of the nanosheet in (g) after a V-shaped notch was fabricated at its upper edge. (i) TEM image of the nanosheet after it was fractured from the notch tip. (j) Schematic of fracture toughness testing setup. (k) HRTEM image of the framed area in (g). (l) Force curve recorded during the nanosheet fracture testing. Reprinted with permission from Ref. 135, Copyright 2015, American Chemical Society.

https://doi.org/10.1557/jmr.2015.304 Published online by Cambridge University Press

Wei et al.[135] first reported the in situ fracture of single-edged V/U–notched multilayer graphene and BN in HRTEM. As shown in Fig. 15(g), a graphene nanosheet was clamped between a force-sensing cantilever (AFM tip) and a movable W tip at its upper edge. A V-shaped notch was made at the middle of the clamped edge by a 300 keV focused electron probe [Fig. 15(h)]. The W tip retracted at a constant speed to fracture the nanosheet from the V-notch tip into two pieces [Fig. 15(i)]. The tension force measured in real-time, increased linearly to 1210 nN and then abruptly dropped to zero [Fig. 15(l)].

With the assistance of in situ TEM measurements, both synthesis and property characterization can be simultaneously realized inside the TEM, which is significant in guiding 2D materials design with novel properties for future development.

VI. SUMMARY AND OUTLOOK

With the rapid development of TEM technology and specialized specimen holders, TEM is utilized not only for imaging and characterizing but also as a nanolab for materials. By introducing various external fields, such as electron irradiation, thermal excitation, electrical field, and mechanical force, into TEM, its rich potential for simulating real environment is unrivalled by any other techniques. However, there are still great inherent limitations. In situ TEM makes it feasible to monitor the dynamic process of chemical reaction and structural evolution at atomic resolution in real time and understand the essential relationship of structures and properties. Since the emerging of 2D materials with extraordinary properties, TEM will definitely have a revolutionary effect on the future development of novel materials. However, there are many inherent limitations of TEM which need to further overcome, like the small sample size, lack of supporting substrates, and difficult to simulate competitive environment. Although a large amount of in situ experiments have been carried out to investigate the structure and structure–property relationship of 2D materials, little is known about the chemistry, bonding, photonic response, and electrical and magnetic properties of TEM. Many challenges exist for the further investigation of the novel 2D materials.

For future work, improving the TEM technology is necessary to achieve ultrahigh spatial and temporal resolution so that each transient moment can be captured during the dynamic material processes. The changes in chemical components and bonding need to be recorded as well. Furthermore, in situ TEM needs to simulate more complicated environments (gas, liquid, and solid) with multiple stimuli (e.g., electromagnetic field, tunable light, and mechanical stress) and simultaneously measure multiple properties (Fig. 16).

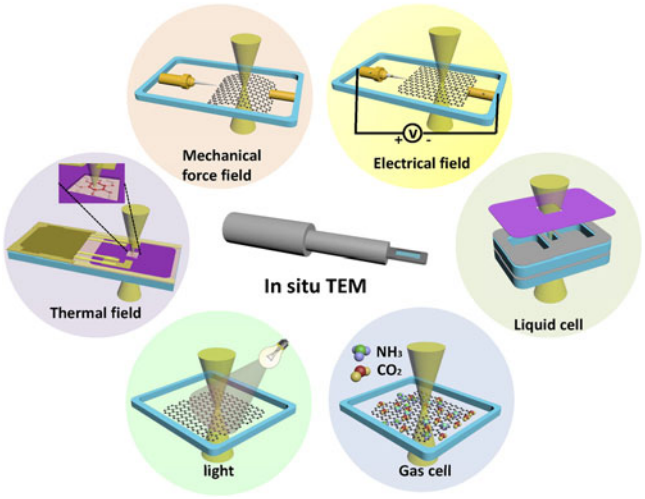


FIG. 16. Future in situ TEM will simulate more complicated environments (gas, liquid, and solid) with multiple stimuli (e.g., electrical field, thermal field, light, and mechanical stress) and simultaneously measure multiple properties.

With the assistance of rapidly advanced in situ TEM technology, new 2D materials with novel functionality can be discovered and an in-depth understanding on how material structure, composition, bonding, and property evolve at atomic resolution under real environments with complex external fields can be obtained. Results of this study can be used to manipulate and engineer 2D materials at the atomic scale with desired structures and properties for different creative applications.

ACKNOWLEDGMENTS

This work was supported by the National Natural Science Foundation of China (Nos. 51420105003, 61274114 and 113279028), the Natural Science Foundation and Qing Lan Project of Jiangsu Province (Nos. BK2011592, BK2012024).

REFERENCES

1. K.S. Novoselov, A.K. Geim, S.V. Morozov, D. Jiang, Y. Zhang, S.V. Dubonos, I.V. Grigorieva, and A.A. Firsov: Electric field effect in atomically thin carbon films. *Science* **306**(5696), 666 (2004).
2. A.K. Geim: Graphene: Status and prospects. *Science* **324**(5934), 1530 (2009).
3. K.S. Novoselov, V.I. Fal'ko, L. Colombo, P.R. Gellert, M.G. Schwab, and K. Kim: A roadmap for graphene. *Nature* **490**(7419), 192 (2012).
4. W-Q. Han, L. Wu, Y. Zhu, K. Watanabe, and T. Taniguchi: Structure of chemically derived mono- and few-atomic-layer boron nitride sheets. *Appl. Phys. Lett.* **93**, 223103 (2008).
5. Z. Zeng, Z. Yin, X. Huang, H. Li, Q. He, G. Lu, F. Boey, and H. Zhang: Single-layer semiconducting nanosheets: High-yield preparation and device fabrication. *Angew. Chem. Int. Ed.* **50**(47), 11093 (2011).
6. M. Xu, T. Liang, M. Shi, and H. Chen: Graphene-like two-dimensional materials. *Chem. Rev.* **113**(5), 3766 (2013).

https://doi.org/10.1557/jmr.2015.304 Published online by Cambridge University Press

7. B. Freitag, S. Kujawa, P.M. Mul, J. Ringnalda, and P.C. Tiemeijer: Breaking the spherical and chromatic aberration barrier in transmission electron microscopy. *Ultramicroscopy* **102**(3), 209 (2005).
8. M. Haider, S. Uhlemann, E. Schwan, H. Rose, B. Kabius, and K. Urban: Electron microscopy image enhanced. *Nature* **392** (6678), 768 (1998).
9. J.L. Hutchison, J.M. Titchmarsh, D.J. Cockayne, R.C. Doole, C.J. Hetherington, A.I. Kirkland, and H. Sawada: A versatile double aberration-corrected, energy filtered HREM/STEM for materials science. *Ultramicroscopy* **103**(1), 7 (2005).
10. C.O. Girit, J.C. Meyer, R. Erni, M.D. Rossell, C. Kisielowski, L. Yang, C-H. Park, M.F. Crommie, M.L. Cohen, S.G. Louie, and A. Zettl: Graphene at the edge: Stability and dynamics. *Science* **323**(5922), 1705 (2009).
11. P. Koskinen, S. Malola, and H. Häkkinen: Evidence for graphene edges beyond zigzag and armchair. *Phys. Rev. B.* **80**, 073401 (2009).
12. J.H. Warner, M.H. Ruemmeli, A. Bachmatiuk, and B. Buechner: Atomic resolution imaging and topography of boron nitride sheets produced by chemical exfoliation. *ACS Nano* **4**(3), 1299 (2010).
13. O. Lehtinen, S. Kurasch, A.V. Krasheninnikov, and U. Kaiser: Atomic scale study of the life cycle of a dislocation in graphene from birth to annihilation. *Nat. Commun.* **4**, 2098 (2013).
14. J.C. Meyer, C. Kisielowski, R. Erni, M.D. Rossell, M.F. Crommie, and A. Zettl: Direct imaging of lattice atoms and topological defects in graphene membranes. *Nano Lett.* **8**(11), 3582 (2008).
15. J.H. Warner, E.R. Margine, M. Mukai, A.W. Robertson, F. Giustino, and A.I. Kirkland: Dislocation-driven deformations in graphene. *Science* **337**(6091), 209 (2012).
16. J. Lin, O. Cretu, W. Zhou, K. Suenaga, D. Prasai, K.I. Bolotin, N.T. Cuong, M. Otani, S. Okada, A.R. Lupini, J.C. Idrobo, D. Caudel, A. Burger, N.J. Ghimire, J. Yan, D.G. Mandrus, S.J. Pennycook, and S.T. Pantelides: Flexible metallic nanowires with self-adaptive contacts to semiconducting transition-metal dichalcogenide monolayers. *Nat. Nanotechnol.* **9**(6), 436 (2014).
17. X. Liu, T. Xu, X. Wu, Z. Zhang, J. Yu, H. Qiu, J-H. Hong, C-H. Jin, J-X. Li, X-R. Wang, L-T. Sun, and W. Guo: Top-down fabrication of sub-nanometre semiconducting nanoribbons derived from molybdenum disulfide sheets. *Nat. Commun.* **4**, 1776 (2013).
18. A. Ziegler, H. Graafsma, X. Zhang, and J.W.M. Frenken: *In-situ Materials Characterization: Across Spatia and Temporal Scales* (Springer, Dordrecht, Netherlands, 2014).
19. B. Barwick, H.S. Park, O-H. Kwon, J.S. Baskin, and A.H. Zewail: 4D imaging of transient structures and morphologies in ultrafast electron microscopy. *Science* **322**(5905), 1227 (2008).
20. F. Carbone, O-H. Kwon, and A.H. Zewail: Dynamics of chemical bonding mapped by energy-resolved 4D electron microscopy. *Science* **325**(5937), 181 (2009).
21. A.H. Zewail: Four-dimensional electron microscopy. *Science* **328**(5975), 187 (2010).
22. U.J. Lorenz and A.H. Zewail: Observing liquid flow in nanotubes by 4D electron microscopy. *Science* **344**(6191), 1496 (2014).
23. R.M. van der Veen, O.H. Kwon, A. Tissot, A. Hauser, and A.H. Zewail: Single-nanoparticle phase transitions visualized by four-dimensional electron microscopy. *Nat. Chem.* **5**(5), 395 (2013).
24. A.W. Robertson, C.S. Allen, Y.A. Wu, K. He, J. Olivier, J. Neethling, A.I. Kirkland, and J.H. Warner: Spatial control of defect creation in graphene at the nanoscale. *Nat. Commun.* **3**, 1144 (2012).
25. J.N. Coleman, M. Lotya, A. O'Neill, S.D. Bergin, P.J. King, U. Khan, K. Young, A. Gaucher, S. De, R.J. Smith, I.V. Shvets, S.K. Arora, G. Stanton, H-Y. Kim, K. Lee, G.T. Kim, G.S. Duesberg, T. Hallam, J.J. Boland, J.J. Wang, J.F. Donegan, J.C. Grunlan, G. Moriarty, A. Shmeliov, R.J. Nicholls, J.M. Perkins, E.M. Grieveson, K. Theuwissen, D.W. McComb, P.D. Nellist, and V. Nicolosi: Two-dimensional nanosheets produced by liquid exfoliation of layered materials. *Science* **331**(6017), 568 (2011).
26. S. Najmaei, Z. Liu, W. Zhou, X. Zou, G. Shi, S. Lei, B.I. Yakobson, J.C. Idrobo, P.M. Ajayan, and J. Lou: Vapour phase growth and grain boundary structure of molybdenum disulphide atomic layers. *Nat. Mater.* **12**(8), 754 (2013).
27. A. Berkdemir, H.R. Gutierrez, A.R. Botello-Mendez, N. Perea-Lopez, A.L. Elias, C-I. Chia, B. Wang, V.H. Crespi, F. Lopez-Urias, J-C. Charlier, H. Terrones, and M. Terrones: Identification of individual and few layers of WS using Raman spectroscopy. *Sci. Rep.* **3**, 1755 (2013).
28. A. Bachmatiuk, R.F. Abelin, H.T. Quang, B. Trzebicka, J. Eckert, and M.H. Rummeli: Chemical vapor deposition of twisted bilayer and few-layer $MoSe_2$ over SiO_x substrates. *Nanotechnology* **25**(36), 365603 (2014).
29. N. Alem, R. Erni, C. Kisielowski, M.D. Rossell, W. Gannett, and A. Zettl: Atomically thin hexagonal boron nitride probed by ultrahigh-resolution transmission electron microscopy. *Phys. Rev. B* **80**, 155425 (2009).
30. C. Jin, F. Lin, K. Suenaga, and S. Iijima: Fabrication of a freestanding boron nitride single layer and its defect assignments. *Phys. Rev. Lett.* **102**, 195505 (2009).
31. K. Davami, M. Shaygan, N. Kheirabi, J. Zhao, D.A. Kovalenko, M.H. Ruemmeli, J. Opitz, G. Cuniberti, J-S. Lee, and M. Meyyappan: Synthesis and characterization of carbon nanowalls on different substrates by radio frequency plasma enhanced chemical vapor deposition. *Carbon* **72**, 372 (2014).
32. H-P. Komsa, J. Kotakoski, S. Kurasch, O. Lehtinen, U. Kaiser, and A.V. Krasheninnikov: Two-dimensional transition metal dichalcogenides under electron irradiation: Defect production and doping. *Phys. Rev. Lett.* **109**, 035503 (2012).
33. T. Bjorkman, S. Kurasch, O. Lehtinen, J. Kotakoski, O.V. Yazyev, A. Srivastava, V. Skakalova, J.H. Smet, U. Kaiser, and A.V. Krasheninnikov: Defects in bilayer silica and graphene: Common trends in diverse hexagonal two-dimensional systems. *Sci. Rep.* **3**, 3482 (2013).
34. J. Kotakoski, A.V. Krasheninnikov, U. Kaiser, and J.C. Meyer: From point defects in graphene to two-dimensional amorphous carbon. *Phys. Rev. Lett.* **106**, 105505 (2011).
35. A.L. Gibb, N. Alem, J.H. Chen, K.J. Erickson, J. Ciston, A. Gautam, M. Linck, and A. Zettl: Atomic resolution imaging of grain boundary defects in monolayer chemical vapor deposition-grown hexagonal boron nitride. *J. Am. Chem. Soc.* **135**(18), 6758 (2013).
36. O. Cretu, Y.C. Lin, and K. Suenaga: Evidence for active atomic defects in monolayer hexagonal boron nitride: A new mechanism of plasticity in two-dimensional materials. *Nano Lett.* **14**(2), 1064 (2014).
37. J.C. Meyer, A. Chuvilin, G. Algara-Siller, J. Biskupek, and U. Kaiser: Selective sputtering and atomic resolution imaging of atomically thin boron nitride membranes. *Nano Lett.* **9**(7), 2683 (2009).
38. H-P. Komsa, S. Kurasch, O. Lehtinen, U. Kaiser, and A.V. Krasheninnikov: From point to extended defects in two-dimensional MoS_2: Evolution of atomic structure under electron irradiation. *Phys. Rev. B.* **88**, 035301 (2013).
39. H. Qiu, T. Xu, Z. Wang, W. Ren, H. Nan, Z. Ni, Q. Chen, S. Yuan, F. Miao, F. Song, G. Long, Y. Shi, L. Sun, J. Wang, and X. Wang: Hopping transport through defect-induced localized states in molybdenum disulphide. *Nat. Commun.* **4**, 2642 (2013).
40. R. Grantab, V.B. Shenoy, and R.S. Ruoff: Anomalous strength characteristics of Tilt grain boundaries in graphene. *Science* **330**(6006), 946 (2010).

https://doi.org/10.1557/jmr.2015.304 Published online by Cambridge University Press

41. P.Y. Huang, C.S. Ruiz-Vargas, A.M. van der Zande, W.S. Whitney, M.P. Levendorf, J.W. Kevek, S. Garg, J.S. Alden, C.J. Hustedt, Y. Zhu, J. Park, P.L. McEuen, and D.A. Muller: Grains and grain boundaries in single-layer graphene atomic patchwork quilts. *Nature* **469**(7330), 389 (2011).
42. A.W. Tsen, L. Brown, M.P. Levendorf, F. Ghahari, P.Y. Huang, R.W. Havener, C.S. Ruiz-Vargas, D.A. Muller, P. Kim, and J. Park: Tailoring electrical transport across grain boundaries in polycrystalline graphene. *Science* **336**(6085), 1143 (2012).
43. J.H. Warner, M. Mukai, and A.I. Kirkland: Atomic structure of ABC rhombohedral stacked trilayer graphene. *ACS Nano* **6**(6), 5680 (2012).
44. C. Cong, K. Li, X.X. Zhang, and T. Yu: Visualization of arrangements of carbon atoms in graphene layers by Raman mapping and atomic-resolution TEM. *Sci. Rep.* **3**, 1195 (2013).
45. R.F. Egerton, P. Li, and M. Malac: Radiation damage in the TEM and SEM. *Micron* **35**(6), 399 (2004).
46. F. Banhart: Irradiation effects in carbon nanostructures. *Rep. Prog. Phys.* **62**(8), 1181 (1999).
47. J.C. Meyer, F. Eder, S. Kurasch, V. Skakalova, J. Kotakoski, H.J. Park, S. Roth, A. Chuvilin, S. Eyhusen, G. Benner, A.V. Krasheninnikov, and U. Kaiser: Accurate measurement of electron beam induced displacement cross sections for single-layer graphene. *Phys. Rev. Lett.* **108**, 196102 (2012).
48. A.W. Robertson and J.H. Warner: Atomic resolution imaging of graphene by transmission electron microscopy. *Nanoscale* **5**(10), 4079 (2013).
49. J. Kotakoski, C. Mangler, and J.C. Meyer: Imaging atomic-level random walk of a point defect in graphene. *Nat. Commun.* **5**, 3991 (2014).
50. J-H. Chen, L. Li, W.G. Cullen, E.D. Williams, and M.S. Fuhrer: Tunable Kondo effect in graphene with defects. *Nat. Phys.* **7**(7), 535 (2011).
51. L. Li, S. Reich, and J. Robertson: Defect energies of graphite: Density-functional calculations. *Phys. Rev. B.* **72**, 184109 (2005).
52. C.J. Russo and J.A. Golovchenko: Atom-by-atom nucleation and growth of graphene nanopores. *Proc. Natl. Acad. Sci. U. S. A.* **109**(16), 5953 (2012).
53. A.W. Robertson, G.D. Lee, K. He, E. Yoon, A.I. Kirkland, and J.H. Warner: Stability and dynamics of the tetravacancy in graphene. *Nano Lett.* **14**(3), 1634 (2014).
54. M. Hjort and S. Stafstrom: Modeling vacancies in graphite via the Huckel method. *Phys. Rev. B.* **61**(20), 14089 (2000).
55. Y. Kim, J. Ihm, E. Yoon, and G.D. Lee: Dynamics and stability of divacancy defects in graphene. *Phys. Rev. B.* **84**, 075445 (2011).
56. A.W. Robertson, K. He, A.I. Kirkland, and J.H. Warner: Inflating graphene with atomic scale blisters. *Nano Lett.* **14**(2), 908 (2014).
57. A.W. Robertson, B. Montanari, K. He, J. Kim, C.S. Allen, Y.A. Wu, J. Olivier, J. Neethling, N. Harrison, A.I. Kirkland, and J.H. Warner: Dynamics of single Fe atoms in graphene vacancies. *Nano Lett.* **13**(4), 1468 (2013).
58. H. Wang, Q. Wang, Y. Cheng, K. Li, Y. Yao, Q. Zhang, C. Dong, P. Wang, U. Schwingenschloegl, W. Yang, and X.X. Zhang: Doping monolayer graphene with single atom substitutions. *Nano Lett.* **12**(1), 141 (2012).
59. Y. Liu and B.I. Yakobson: Cones, pringles, and grain boundary landscapes in graphene topology. *Nano Lett.* **10**(6), 2178 (2010).
60. S. Malola, H. Häkkinen, and P. Koskinen: Structural, chemical, and dynamical trends in graphene grain boundaries. *Phys. Rev. B.* **81**, 165447 (2010).
61. O.V. Yazyev and S.G. Louie: Topological defects in graphene: Dislocations and grain boundaries. *Phys. Rev. B.* **81**, 195420 (2010).
62. O.V. Yazyev and S.G. Louie: Electronic transport in polycrystalline graphene. *Nat. Mater.* **9**(10), 806 (2010).
63. J. An, E. Voelkl, J.W. Suk, X. Li, C.W. Magnuson, L. Fu, P. Tiemeijer, M. Bischoff, B. Freitag, E. Popova, and R.S. Ruoff: Domain (grain) boundaries and evidence of "twinlike" structures in chemically vapor deposited grown graphene. *ACS Nano* **5**(4), 2433 (2011).
64. K. Kim, Z. Lee, W. Regan, C. Kisielowski, M.F. Crommie, and A. Zettl: Grain boundary mapping in polycrystalline graphene. *ACS Nano.* **5**(3), 2142 (2011).
65. A.W. Robertson, A. Bachmatiuk, Y.A. Wu, F. Schaeffel, B. Rellinghaus, B. Buechner, M.H. Ruemmeli, and J.H. Warner: Atomic structure of interconnected few-layer graphene domains. *ACS Nano.* **5**(8), 6610 (2011).
66. S. Kurasch, J. Kotakoski, O. Lehtinen, V. Skákalová, J. Smet, C.E. Krill, A.V. Krasheninnikov, and U. Kaiser: Atom-by-atom observation of grain boundary migration in graphene. *Nano Lett.* **12**(6), 3168 (2012).
67. D.J. Klein: Graphitic polymer strips with edge states. *Chem. Phys. Lett.* **217**(3), 261 (1994).
68. J. Kotakoski, D. Santos-Cottin, and A.V. Krasheninnikov: Stability of graphene edges under electron beam: Equilibrium energetics versus dynamic effects. *ACS Nano* **6**(1), 671 (2012).
69. P. Koskinen, S. Malola, and H. Häkkinen: Self-passivating edge reconstructions of graphene. *Phys. Rev. Lett.* **101**, 115502 (2008).
70. K. Kim, S. Coh, C. Kisielowski, M.F. Crommie, S.G. Louie, M.L. Cohen, and A. Zettl: Atomically perfect torn graphene edges and their reversible reconstruction. *Nat. Commun.* **4**, 2723 (2013).
71. J.H. Warner, M.H. Ruemmeli, L. Ge, T. Gemming, B. Montanari, N.M. Harrison, B. Buechner, and G.A.D. Briggs: Structural transformations in graphene studied with high spatial and temporal resolution. *Nat. Nanotechnol.* **4**(8), 500 (2009).
72. T. Kawai, Y. Miyamoto, O. Sugino, and Y. Koga: Graphitic ribbons without hydrogen-termination: Electronic structures and stabilities. *Phys. Rev. B.* **62**(24), R16349 (2000).
73. K. He, G.D. Lee, A.W. Robertson, E. Yoon, and J.H. Warner: Hydrogen-free graphene edges. *Nat. Commun.* **5**, 3040 (2014).
74. Z. Liu, K. Suenaga, P.J.F. Harris, and S. Iijima: Open and closed edges of graphene layers. *Phys. Rev. Lett.* **102**, 015501 (2009).
75. B. Westenfelder, J.C. Meyer, J. Biskupek, S. Kurasch, F. Scholz, C.E. Krill, III, and U. Kaiser: Transformations of carbon adsorbates on graphene substrates under extreme heat. *Nano Lett.* **11**(12), 5123 (2011).
76. K. Watanabe, T. Taniguchi, and H. Kanda: Direct-bandgap properties and evidence for ultraviolet lasing of hexagonal boron nitride single crystal. *Nat. Mater.* **3**(6), 404 (2004).
77. O.L. Krivanek, M.F. Chisholm, V. Nicolosi, T.J. Pennycook, G.J. Corbin, N. Dellby, M.F. Murfitt, C.S. Own, Z.S. Szilagyi, M.P. Oxley, S.T. Pantelides, and S.J. Pennycook: Atom-by-atom structural and chemical analysis by annular dark-field electron microscopy. *Nature* **464**(7288), 571 (2010).
78. A. Zobelli, A. Gloter, C.P. Ewels, G. Seifert, and C. Colliex: Electron knock-on cross section of carbon and boron nitride nanotubes. *Phys. Rev. B.* **75**, 245402 (2007).
79. G. Giovannetti, P.A. Khomyakov, G. Brocks, P.J. Kelly, and J. van den Brink: Substrate-induced band gap in graphene on hexagonal boron nitride: Ab initio density functional calculations. *Phys. Rev. B.* **76**, 073103 (2007).
80. J. Brivio, D.T.L. Alexander, and A. Kis: Ripples and layers in ultrathin MoS_2 membranes. *Nano Lett.* **11**(12), 5148 (2011).
81. K.F. Mak, C. Lee, J. Hone, J. Shan, and T.F. Heinz: Atomically thin MoS_2: A new direct-gap semiconductor. *Phys. Rev. Lett.* **105**, 136805 (2010).
82. A. Splendiani, L. Sun, Y. Zhang, T. Li, J. Kim, C-Y. Chim, G. Galli, and F. Wang: Emerging photoluminescence in monolayer MoS_2. *Nano Lett.* **10**(4), 1271 (2010).

https://doi.org/10.1557/jmr.2015.304 Published online by Cambridge University Press

83. W. Zhou, X. Zou, S. Najmaei, Z. Liu, Y. Shi, J. Kong, J. Lou, P.M. Ajayan, B.I. Yakobson, and J.C. Idrobo: Intrinsic structural defects in monolayer molybdenum disulfide. *Nano Lett.* **13**(6), 2615 (2013).
84. G.D. Lee, C.Z. Wang, E. Yoon, N.M. Hwang, D.Y. Kim, and K.M. Ho: Diffusion, coalescence, and reconstruction of vacancy defects in graphene layers. *Phys. Rev. Lett.* **95**, 205501 (2005).
85. J.A. Rodriguez-Manzo, C. Pham-Huu, and F. Banhart: Graphene growth by a metal-catalyzed solid-state transformation of amorphous carbon. *ACS Nano.* **5**(2), 1529 (2011).
86. L. He, T. Xu, J. Sun, K. Yin, X. Xie, L. Ding, H. Xiu, and L. Sun: Investment casting of carbon tubular structures. *Carbon* **50**(8), 2845 (2012).
87. A. Barreiro, F. Börrnert, S.M. Avdoshenko, B. Rellinghaus, G. Cuniberti, M.H. Rümmeli, and L.M.K. Vandersypen: Understanding the catalyst-free transformation of amorphous carbon into graphene by current-induced annealing. *Sci. Rep.* **3**, 1115 (2013).
88. Z. Liu, Y.C. Lin, C.C. Lu, C.H. Yeh, P.W. Chiu, S. Iijima, and K. Suenaga: In-situ observation of step-edge in-plane growth of graphene in a STEM. *Nat. Commun.* **5**, 4055 (2014).
89. J. Zhao, Q. Deng, A. Bachmatiuk, G. Sandeep, A. Popov, J. Eckert, and M.H. Ruemmeli: Free-standing single-atom-thick iron membranes suspended in graphene pores. *Science* **343**(6176), 1228 (2014).
90. F.B. Romdhane, T. Bjoerkman, J.A. Rodriguez-Manzo, O. Cretu, A.V. Krasheninnikov, and F. Banhart: In situ growth of cellular two-dimensional silicon oxide on metal substrates. *ACS Nano* **7**(6), 5175 (2013).
91. F. Ben Romdhane, T. Björkman, A.V. Krasheninnikov, and F. Banhart: Solid-state growth of one- and two-dimensional silica structures on metal surfaces. *J. Phys. Chem. C* **118**(36), 21001 (2014).
92. Y. Gan, L. Sun, and F. Banhart: One- and two-dimensional diffusion of metal atoms in graphene. *Small* **4**(5), 587 (2008).
93. H. Wang, K. Li, Y. Cheng, Q. Wang, Y. Yao, U. Schwingenschlogl, X. Zhang, and W. Yang: Interaction between single gold atom and the graphene edge: A study via aberration-corrected transmission electron microscopy. *Nanoscale* **4**(9), 2920 (2012).
94. J.A. Rodriguez-Manzo, O. Cretu, and F. Banhart: Trapping of metal atoms in vacancies of carbon nanotubes and graphene. *ACS Nano.* **4**(6), 3422 (2010).
95. O. Cretu, A.V. Krasheninnikov, J.A. Rodriguez-Manzo, L. Sun, R.M. Nieminen, and F. Banhart: Migration and localization of metal atoms on strained graphene. *Phys. Rev. Lett.* **105**, 196102 (2010).
96. Z. He, K. He, A.W. Robertson, A.I. Kirkland, D. Kim, J. Ihm, E. Yoon, G-D. Lee, and J.H. Warner: Atomic structure and dynamics of metal dopant pairs in graphene. *Nano Lett.* **14**(7), 3766 (2014).
97. W. Zhou, M.D. Kapetanakis, M.P. Prange, S.T. Pantelides, S.J. Pennycook, and J-C. Idrobo: Direct determination of the chemical bonding of individual impurities in graphene. *Phys. Rev. Lett.* **109**, 206803 (2012).
98. J. Lee, W. Zhou, S.J. Pennycook, J.C. Idrobo, and S.T. Pantelides: Direct visualization of reversible dynamics in a Si(6) cluster embedded in a graphene pore. *Nat. Commun.* **4**, 1650 (2013).
99. A.V. Krasheninnikov, P.O. Lehtinen, A.S. Foster, P. Pyykko, and R.M. Nieminen: Embedding transition-metal atoms in graphene: Structure, bonding, and magnetism. *Phys. Rev. Lett.* **102**, 126807 (2009).
100. W.L. Wang, E.J.G. Santos, B. Jiang, E.D. Cubuk, C. Ophus, A. Centeno, A. Pesquera, A. Zurutuza, J. Ciston, R. Westervelt, and E. Kaxiras: Direct observation of a long-lived single-atom catalyst chiseling atomic structures in graphene. *Nano Lett.* **14**(2), 450 (2014).
101. X. Wei, M-S. Wang, Y. Bando, and D. Golberg: Electron-beam-induced substitutional carbon doping of boron nitride nanosheets, nanoribbons, and nanotubes.*ACS Nano.* **5**(4), 2916 (2011).
102. A.J. Storm, J.H. Chen, X.S. Ling, H.W. Zandbergen, and C. Dekker: Fabrication of solid-state nanopores with single-nanometre precision. *Nat. Mater.* **2**(8), 537 (2003).
103. T. Xu, K. Yin, X. Xie, L. He, B. Wang, and L. Sun: Size-dependent evolution of graphene nanopores under thermal excitation. *Small* **8**(22), 3422 (2012).
104. M.J. Kim, B. McNally, K. Murata, and A. Meller: Characteristics of solid-state nanometre pores fabricated using a transmission electron microscope. *Nanotechnology* **18**(20), 205302 (2007).
105. T. Xu, X. Xie, K. Yin, J. Sun, L. He, and L. Sun: Controllable atomic-scale sculpting and deposition of carbon nanostructures on graphene. *Small* **10**(9), 1724 (2014).
106. S. Wu, F. Cao, H. Zheng, H. Sheng, C. Liu, Y. Liu, D. Zhao, and J. Wang: Fabrication of faceted nanopores in magnesium. *Appl. Phys. Lett.* **103**(24), 243101 (2013).
107. H. Zheng, Y. Liu, F. Cao, S. Wu, S. Jia, A. Cao, D. Zhao, and J. Wang: Electron beam-assisted healing of nanopores in magnesium alloys. *Sci. Rep.* **3**, 1920 (2013).
108. B. Song, G.F. Schneider, Q. Xu, G. Pandraud, C. Dekker, and H. Zandbergen: Atomic-scale electron-beam sculpting of near-defect-free graphene nanostructures. *Nano Lett.* **11**(6), 2247 (2011).
109. A.V. Krasheninnikov and F. Banhart: Engineering of nanostructured carbon materials with electron or ion beams. *Nat. Mater.* **6**(10), 723 (2007).
110. A. Chuvilin, J.C. Meyer, G. Algara-Siller, and U. Kaiser: From graphene constrictions to single carbon chains. *New J. Phys.* **11**, 083109 (2009).
111. C. Jin, H. Lan, L. Peng, K. Suenaga, and S. Iijima: Deriving carbon atomic chains from graphene. *Phys. Rev. Lett.* **102**, 205501 (2009).
112. M.D. Fischbein and M. Drndić: Electron beam nanosculpting of suspended graphene sheets. *Appl. Phys. Lett.* **93**(11), 113107 (2008).
113. X. Jia, M. Hofmann, V. Meunier, B.G. Sumpter, J. Campos-Delgado, J.M. Romo-Herrera, H. Son, Y-P. Hsieh, A. Reina, J. Kong, M. Terrones, and M.S. Dresselhaus: Controlled formation of sharp zigzag and armchair edges in graphitic nanoribbons. *Science* **323**(5922), 1701 (2009).
114. K.A. Ritter and J.W. Lyding: The influence of edge structure on the electronic properties of graphene quantum dots and nanoribbons. *Nat. Mater.* **8**(3), 235 (2009).
115. O. Cretu, A.R. Botello-Mendez, I. Janowska, P-H. Cuong, J-C. Charlier, and F. Banhart: Electrical transport measured in atomic carbon chains. *Nano Lett.* **13**(8), 3487 (2013).
116. J.H. Warner, Y. Fan, A.W. Robertson, K. He, E. Yoon, and G.D. Lee: Rippling graphene at the nanoscale through dislocation addition. *Nano Lett.* **13**(10), 4937 (2013).
117. J. Chen, T. Shi, T. Cai, T. Xu, L. Sun, X. Wu, and D. Yu: Self healing of defected graphene. *Appl. Phys. Lett.* **102**(10), 103107 (2013).
118. X. He, T. Xu, X. Xu, Y. Zeng, J. Xu, L. Sun, C. Wang, H. Xing, B. Wu, A. Lu, D. Liu, X. Chen, and J. Chu: In-situ atom scale visualization of domain wall dynamics in VO_2 insulator-metal phase transition. *Sci. Rep.* **4**, 6544 (2014).
119. Y-C. Lin, D.O. Dumcenco, Y-S. Huang, and K. Suenaga: Atomic mechanism of the semiconducting-to-metallic phase transition in single-layered MoS_2. *Nat. Nanotechnol.* **9**(5), 391 (2014).
120. G. Eda, T. Fujita, H. Yamaguchi, D. Voiry, M. Chen, and M. Chhowalla: Coherent atomic and electronic heterostructures of single-layer MoS_2. *ACS Nano.* **6**(8), 7311 (2012).

https://doi.org/10.1557/jmr.2015.304 Published online by Cambridge University Press

121. A. Barreiro, F. Borrnert, M.H. Rummeli, B. Buchner, and L.M. Vandersypen: Graphene at high bias: Cracking, layer by layer sublimation, and fusing. *Nano Lett.* **12**(4), 1873 (2012).
122. F. Borrnert, A. Barreiro, D. Wolf, M.I. Katsnelson, B. Buchner, L.M.K. Vandersypen, and M.H. Rummeli: Lattice expansion in seamless bilayer graphene constrictions at high bias. *Nano Lett.* **12**(9), 4455 (2012).
123. J.Y. Huang, F. Ding, B.I. Yakobson, P. Lu, L. Qi, and J. Li: In-situ observation of graphene sublimation and multi-layer edge reconstructions. *Proc. Natl. Acad. Sci. U. S. A.* **106**(25), 10103 (2009).
124. A.L. Torre, A. Botello-Mendez, W. Baaziz, J.C. Charlier, and F. Banhart: Strain-induced metal-semiconductor transition observed in atomic carbon chains. *Nat. Commun.* **6**, 6636 (2015).
125. Y. Lu, C.A. Merchant, M. Drndic, and A.T.C. Johnson: In-situ electronic characterization of graphene nanoconstrictions fabricated in a transmission electron microscope. *Nano Lett.* **11**(12), 5184 (2011).
126. M.S. Wang, D. Golberg, and Y. Bando: Tensile tests on individual single-walled carbon nanotubes: Linking nanotube strength with its defects. *Adv. Mater.* **22**(36), 4071 (2010).
127. H. Zheng, A. Cao, C.R. Weinberger, J.Y. Huang, K. Du, J. Wang, Y. Ma, Y. Xia, and S.X. Mao: Discrete plasticity in sub-10-nm-sized gold crystals. *Nat. Commun.* **1**, 144 (2010).
128. J.W. Wang, S. Narayanan, J.Y. Huang, Z. Zhang, T. Zhu, and S.X. Mao: Atomic-scale dynamic process of deformation-induced stacking fault tetrahedra in gold nanocrystals. *Nat. Commun.* **4**, 2340 (2013).
129. J. Sun, L. He, Y.C. Lo, T. Xu, H. Bi, L. Sun, Z. Zhang, S.X. Mao, and J. Li: Liquid-like pseudoelasticity of sub-10-nm crystalline silver particles. *Nat. Mater.* **13**(11), 1007 (2014).
130. X.D. Han, Y.F. Zhang, K. Zheng, X.N. Zhang, Z. Zhang, Y.J. Hao, X.Y. Guo, J. Yuan, and Z.L. Wang: Low-temperature in-situ large strain plasticity of ceramic SiC nanowires and its atomic-scale mechanism. *Nano Lett.* **7**(2), 452 (2007).
131. K. Zheng, X.D. Han, L.H. Wang, Y.F. Zhang, Y.H. Yue, Y. Qin, X.N. Zhang, and Z. Zhang: Atomic mechanisms governing the elastic limit and the incipient plasticity of bending Si nanowires. *Nano Lett.* **9**(6), 2471 (2009).
132. K. Zheng, C. Wang, Y.Q. Cheng, Y. Yue, X. Han, Z. Zhang, Z. Shan, S.X. Mao, M. Ye, Y. Yin, and E. Ma: Electron-beam-assisted superplastic shaping of nanoscale amorphous silica. *Nat. Commun.* **1**, 24 (2010).
133. L. Wang, P. Liu, P. Guan, M. Yang, J. Sun, Y. Cheng, A. Hirata, Z. Zhang, E. Ma, M. Chen, and X. Han: In-situ atomic-scale observation of continuous and reversible lattice deformation beyond the elastic limit. *Nat. Commun.* **4**, 2413 (2013).
134. D-M. Tang, D.G. Kvashnin, S. Najmaei, Y. Bando, K. Kimoto, P. Koskinen, P.M. Ajayan, B.I. Yakobson, P.B. Sorokin, J. Lou, and D. Golberg: Nanomechanical cleavage of molybdenum disulphide atomic layers. *Nat. Commun.* **5**, 3631 (2014).
135. X. Wei, S. Xiao, F. Li, D.M. Tang, Q. Chen, Y. Bando, and D. Golberg: Comparative fracture toughness of multilayer graphenes and boronitrenes. *Nano Lett.* **15**(1), 689 (2015).

https://doi.org/10.1557/jmr.2015.304 Published online by Cambridge University Press